OULU 2015
C 532

ACTA UNIVERSITATIS OULUENSIS

Mikko Leinonen

FINITE ELEMENT METHOD AND EQUIVALENT CIRCUIT BASED DESIGN OF PIEZOELECTRIC ACTUATORS AND ENERGY HARVESTER DYNAMICS

UNIVERSITY OF OULU GRADUATE SCHOOL;
UNIVERSITY OF OULU,
FACULTY OF INFORMATION TECHNOLOGY AND ELECTRICAL ENGINEERING,
DEPARTMENT OF ELECTRICAL ENGINEERING

ACTA UNIVERSITATIS OULUENSIS
C Technica 532

MIKKO LEINONEN

FINITE ELEMENT METHOD AND EQUIVALENT CIRCUIT BASED DESIGN OF PIEZOELECTRIC ACTUATORS AND ENERGY HARVESTER DYNAMICS

Academic dissertation to be presented with the assent of the Doctoral Training Committee of Technology and Natural Sciences of the University of Oulu for public defence in the OP auditorium (L10), Linnanmaa, on 26 June 2015, at 12 noon

UNIVERSITY OF OULU, OULU 2015

Acta Univ. Oul. C 532, 2015

Supervised by
Docent Jari Juuti
Professor Heli Jantunen

Reviewed by
Professor Stephen Beeby
Professor Pasi Kallio

ISBN 978-952-62-0836-7 (Paperback)
ISBN 978-952-62-0837-4 (PDF)

ISSN 0355-3213 (Printed)
ISSN 1796-2226 (Online)

Cover Design
Raimo Ahonen

JUVENES PRINT
TAMPERE 2015

Leinonen, Mikko, Finite element method and equivalent circuit based design of piezoelectric actuators and energy harvester dynamics
University of Oulu Graduate School; University of Oulu, Faculty of Information Technology and Electrical Engineering, Department of Electrical Engineering
Acta Univ. Oul. C 532, 2015
University of Oulu, P.O. Box 8000, FI-90014 University of Oulu, Finland

Abstract

The main objective of this thesis was to use and combine Finite Element Method (FEM) and small signal equivalent circuit models in actuator and energy harvesting design and to study the dynamics of the said designs.

The work is divided into four different sections. In the first section, the small signal parameters are derived for a pre-stressed piezoelectric actuator using a series of measurements. In addition, the tunability of the resonance frequency using mass and series capacitors is investigated.

In the second section, a piezoelectric Fabry Perot Interferometer actuator is simulated using FEM and the small signal parameters are derived using FEM simulations. The modelled results are compared with the actual measurements and the resonance frequency is found to differ by only 0.8 percent from the measured values when the mirror is attached to the actuator.

In the third section a piezoelectric wide band energy harvester is developed with multiple beam topology. Two different designs are compared, one produced using the conventional PZT-steel structure and one with a PZT-LTCC structure.

The final section presents an FEM model for a shoe mounted energy harvester and concentrates on the modelling of walking dynamics in FEM. The simulation results are compared to actual measurements and the simulated power values are found to differ by only 7% when the cymbal stroke is below 1.3 mm. The generated model is also expandable to other types of energy harvesters and the methods developed can be used in a variety of different energy harvesting simulations and harvester development.

The results show that the equivalent circuit approach together with FEM modelling is a powerful tool in the dynamics design of piezoelectric actuators and energy harvesters.

Keywords: actuator, energy harvester, FEM, piezoelectric

Leinonen, Mikko, Elementtimenetelmän ja vastinpiirien käyttö pietsosähköisten aktuaattorien ja energiankorjuukomponenttien dynamiikan suunnittelussa
Oulun yliopiston tutkijakoulu; Oulun yliopisto, Tieto- ja sähkötekniikan tiedekunta, Sähkötekniikan osasto
Acta Univ. Oul. C 532, 2015
Oulun yliopisto, PL 8000, 90014 Oulun yliopisto

Tiivistelmä

Väitöstyön päätavoitteena oli yhdistää elementtimenetelmät (FEM) ja piensignaalimallit aktuaattorien ja energiankorjuukomponenttien suunnittelussa ja tutkia niiden dynamiikkaa.

Työ on jaettu neljään eri osaan. Ensimmäisessä osassa piensignaalimallit johdettiin pietsosähköisestä aktuaattorista mittausten avulla. Lisäksi resonanssitaajuuden muuttamista tutkitaan massan ja sarjaan kytketyn kapasitanssin avulla.

Toisessa osassa simuloidaan pietsosähköistä Fabry Perot interferometria käyttäen elementtimenetelmää. Lisäksi komponentin piensignaalimalli luodaan käyttäen simulointimallia. Lopuksi piensignaalimallin ja prototyypin mittaustuloksia verrataan. Mallin resonanssitaajuus poikkeaa mitatusta vain 0.8 %, kun aktuaattoriin on kiinnitetty peili.

Kolmannessa osassa kehitetään ja verrataan toisiinsa kahta erilaista laajakaistaista monipalkkista pietsosähköistä energian korjuukomponenttia. Toinen komponenteista on toteutettu perinteisellä PZT-teräs rakenteella ja toinen yhteissintratulla PZT-LTCC rakenteella.

Viimeisessä osassa luodaan simulaatio malli kenkään asennetulle cymbal tyyppiselle pietsosähköiselle energian korjuukomponentille ja kävelyn dynamiikkaa tutkitaan. Luotua mallia verrataan prototyypin mittaustuloksiin ja simuloitu energian tuotto poikkeaa vain 7 % alle 1.3 mm puristusliikkeellä.

Tulokset osoittivat, että piensignaalimallin ja elementtimenetelmän yhdistäminen on tehokas apu pietsosähköisten aktuaattorien ja energiankorjuukomponenttien dynamiikan suunnittelussa.

Asiasanat: aktuaattori, energiankorjuukomponentti, FEM, pietsosähköisyys

Acknowledgements

First of all, I wish to thank my supervisors Docent Jari Juuti and Professor Heli Jantunen for supervising and supporting my work. Furthermore, I would like to thank the colleagues at Microelectronics and Materials Physics laboratories for a good working environment. Jaakko Palosaari, Maciej Sobocinski and Jari Juuti have been of tremendous help in my work and for that I am grateful. Professor A.E. Hill has also been very helpful in correcting my grammar in this thesis and in our papers.

The Finnish Foundation for Technology Promotion, Wihuri Foundation, KAUTE Foundation and GETA graduate school are acknowledged for financially supporting this work.

Oulu, May 2015 Mikko Leinonen

List of abbreviations and symbols

α	Overlapping factor
ε	Permittivity
ξ	Damping ratio
ν	Poisson's ratio
ω	Angular frequency
AFM	Atomic Force Microscope
BW	Bandwidth
C	Capacitance
C_s	Series capacitance
CST	Constant Strain Triangle
CTE	Coefficient of Thermal Expansion
d	Displacement
e	error
E	Young's modulus
F	Force
FEM	Finite Element Method
FPI	Fabry-Pérot Interferometer
f_{res}	Resonance frequency
GA	Genetic Algorithm
IR	InfraRed
k	Spring constant
k_{eff}	Effective spring constant
l	Length of a beam
LASER	Light Amplification by Stimulated Emission of Radiation
LCR	Inductor, capacitor and resistor circuit
LTCC	Low Temperature Co-fired Ceramic
LVDT	Linear Variable Differential Transformer
m	Mass
m_{added}	Added mass
m_{eff}	Effective mass
MFC	Macro Fiber Composite
n	Transformer turn ratio
NIR	Near InfraRed
PZT	Lead Zirconium Titanate
R_{in}	Input resistance

r_m	Mechanical resistive impedance representing mechanical losses
SOI	Silicon On Insulator
SPICE	Simulation Program with Integrated Circuit Emphasis
V_{in}	Input voltage
$V_{p\text{-}p}$	Peak-to-peak voltage
x	Displacement

List of original papers

This thesis is based on the following five original papers, which are cited in the text by the given roman numerals.

I Leinonen M, Juuti J & Jantunen H (2005) Equivalent circuit based modification of a pre-stressed piezo actuator. Proc. 4th Int. Conf. on Smart Systems, Seinäjoki.

II Sobocinski M, Leinonen M, Juuti J & Jantunen H (2012) A Piezoelectric Active Mirror Suspension System Embedded Into Low-Temperature Cofired Ceramic. IEEE trans. on Ultrasonics, Ferroelectrics and frequency control 59(9): 1990-1995.

III Leinonen M, Palosaari J, Juuti J & Jantunen H (2011) Piezoelectric energy harvester for vibrating environments using multiple beam topology for wideband operation. AP XIX Proceedings 41, Helsinki.

IV Sobocinski M, Leinonen M, Juuti J & Jantunen H (2011) Monomorph piezoelectric wideband energy harvester integrated into LTCC. Journal Of European Ceramic Society 31(5): 789-794.

V Leinonen M, Palosaari J, Juuti J & Jantunen H (2014) Combined electrical and electromechanical simulations of a piezoelectric Cymbal harvester for energy harvesting from walking. Journal of Intelligent Material Systems and Structures, 25(4): 391-400.

In Paper I an equivalent circuit for a piezoelectric actuator is developed using measurements and is then used to tune the resonance frequency of the actuator. In Paper II a mirror suspension actuator is developed on LTCC for IR spectroscopy. In this paper the FEM simulations are used as the main tool in the design. In Paper III a wideband energy harvester is developed with 5 differently tuned piezoelectric beams using a conventional PZT-Steel structure. In Paper IV an improved wideband energy harvester is developed with LTCC technology in order to improve the resonance frequency accuracy. In Paper V an energy harvester for walking is modelled and simulated using FEM software and the results are compared with actual measurements.

In Paper I the idea, measurements and the main part of the writing was done by the author. In Paper II the idea, design and the modelling was done by the author and the manufacturing and measurements were done by co-authors. In paper III the idea, theory and design of the harvester as well as part of the analysis of the results was
done by the author. The manufacturing and the measurements were done by the co-authors. In Paper IV the idea of the energy harvester and the design as well as the main part of the writing was done by the author. The manufacturing and the measurements were done with the help of co-authors. In Paper V the development

of the simulation model, simulations and the main part of the writing were done by the author and the idea and design of the harvester as well as the measurements were done by the co-authors.

Contents

1 Introduction

Piezoelectric actuators, sensors and energy harvesters are widely used in different applications throughout industry and are also encountered in many everyday tasks in people's lives. These piezoelectric components can be categorized as transducers that either transform electrical energy into kinetic energy (actuators) or vice versa (energy harvesters and sensors). The rate of this energy transformation is defined by the mode of actuation, sensing or energy production. These modes can be roughly divided into two operating groups as static and dynamic operation modes. Static or quasistatic operation is encountered in actuation and sensing but usually not in energy harvesting. Dynamic operation, on the other hand, is used in all of the transducer applications. The dynamics of the transducers play an important role in the design of the said components. For example, the actuators and sensors in micropositioning systems should preferably work outside resonance in order to maintain a linear frequency response and avoid ringing. Energy harvesting applications, on the other hand, usually benefit greatly from operating in resonance. Some actuator applications such as ultrasonic actuators are also dependent on operation at resonance frequencies.

1.1 Actuator and energy harvesting dynamics

Piezoelectric actuators come in many sizes and can be used to drive bulky equipment as well as micro- or even nano-scale objects. Applications where large objects are actuated include, for example, telescopes such as in the Japanese Subaru telescope where the mirror is actively suspended, thus avoiding the disadvantages of a rigid mirror [1,2]. Similarly, a telescopic active hexapod utilizes piezoelectric actuators [2,3]. In [4] a method was presented to replace the conventional control surfaces with piezoelectric composite fibres (MFC) embedded into an aircraft wing. A similar concept was presented in [5] with adaptive control implemented using piezoelectric actuators. Piezoelectric actuators are, however, more prominent at the smaller end of the size spectrum. The atomic force microscope (AFM) and scanning probe microscope both utilize piezoelectric actuators in the manipulation of the tip [2,6]. The resolution of these devices is in the nanometre scale and with small scanning areas (5x5x1 μm) the resolution can reach 0.1 nm in the XY-direction and 0.015 nm in the Z-direction [7,8]. The nonlinear nature of the piezoelectric actuators means that, in micropositioning, control systems are needed together with the sensors to

linearize the system. Closed loop control, however, requires that the dynamical properties of the actuator are known in order to guarantee stability. Some open loop control schemes are also viable; for example, current drive, where the effect of the nonlinear capacitance of the piezoelectric component is avoided by using charge as the input. This reduces hysteresis, which can be around 15 % without any control [9], and requires no instrumentation other than metering of the current [9,10]. For example, in [11], the initial hysteresis of 27 % was reduced to only 2 % by using current drive. In current drive the model for the piezoelectric component is not needed, but can be included to improve performance [11]. However, in the case of both open (feed-forward) and closed loop control the model needs to be known. The exception to this is the use of various adaptive control systems, where the parameters of the model are not known *a priori*, but rather generated iteratively during the operation of the device [12].

In some open loop control methods the system is modelled and then the inverse of the model is applied as the controller, thus altering the dynamics and nonlinearities of the system. This method relies on very accurate modelling of the system and in some cases only the nonlinearities are modelled while preserving the dynamical characteristics of the system [2,13]. The hysteresis can be modelled with various methods such as the Preisach model and its variant Prandtl-Ishlinskii models. These models have yielded good results in hysteresis cancellation: for example an uncontrolled error of 17.5 % was reduced to 2 % using the Prandtl-Ishlinskii model in [14].

Closed loop control, by its very nature, requires a feedback signal from the output. For example, in micropositioning applications this signal derives from the displacement of the actuator and in acoustic devices this can be the sound pressure signal from a microphone or hydrophone. The feedback control requires a high quality feedback signal because any interference and noise added to the feedback signal is also treated as an input signal and is therefore usually passed unattenuated to the output. In micropositioning applications the movements are small, usually in the range of a few micrometres or even nanometres, and measuring such small movements makes high demands on the instrumentation of the system. Methods commonly used in conjunction with piezoelectric actuators include Linear Variable Differential Transformer (LVDT), Light Amplification by Stimulated Emission of Radiation (LASER), capacitive, strain gauge and piezoresistive sensors [15-19]. In addition, the model of the system should be known in order to control the system reliably, as is the case with most of the control systems described.

The Finite Element Method (FEM) is traditionally used in mechanical engineering to study the strain and stress in solid material. FEM is therefore well suited for modelling piezoelectrical components and various examples of design based on FEM modelling exist, for example in fuel injector design [20,21]. In energy harvesting FEM modelling can be used to design structures where analytical methods can be too difficult to realize. FEM modelling can also enable optimization with methods such as genetic algorithms (GA) [22].

Small signal models have been traditionally used in electric circuit design, but mechanical systems can be modelled using the same circuit components as in electric circuit models. Piezoelectric components, having both electrical and mechanical components, are therefore well suited for equivalent circuit analysis where lumped circuit parameters represent the mass, spring and losses of the component. The most classical equivalent circuit is the Butterworth Van Dyke circuit [23]. This model is usable when the first resonance mode of the component is under examination and the operation is considered linear. Nonlinearities such as impact can be modelled, for example, by adding nonlinear components to the circuit [24]. In this work, the small signal model is used to study the dynamics of the actuators and to tune the resonance frequency. Nonlinear parameters are encountered in the studied cymbal harvester, and can be used to explain the nonlinear behaviour under high load conditions.

Harvesting energy from vibration is most efficiently done at the resonance frequency of the piezoelectric component, and when designing a wideband energy harvester the resonances have to be designed in such a way as to create a pass-band. This task also requires a knowledge of the dynamics of the vibrating piezoelectric components. This can be acquired by creating a small signal model of the vibrating component. In particular, in multiple beam wideband energy harvesters, the individual beams' resonance frequencies have to be tuned in order to create a wide pass-band. This task requires a knowledge of the beam's dynamics and this can be acquired by creating a small signal model of the beam. With the aid of this model the dynamics can then be designed in such a way that the required wideband operation is achieved. Multiple beam harvesters have been manufactured using electromagnetic [25] and piezoelectric beams [26]. Piezoelectric bimorphs with varying piezoelectric layer thicknesses were used in [27] to achieve the desired resonance frequency distribution. Beam length was varied in [28] and masses were varied in [28,29].

1.2 Scope and outline of the thesis

In this work, small signal models are generated for a multitude of actuators and energy harvesters. The emphasis is on the resonance frequency behaviour and therefore the Butterworth-Van Dyke equivalent circuit is used as the model. The parameters were obtained either by measurements or by FEM-simulations.

In Chapter 2, an equivalent circuit model is obtained for a pre-stressed piezoelectric component. The pre-stressing makes it difficult to obtain the parameters using analytical methods alone and thus they were obtained using a series of measurements.

In Chapter 3, a Fabry-Pérot Interferometer (FPI) actuator is developed and characterized. The dynamics of the mirror actuator are critical in interferometer applications and therefore the dynamical model is required. The model was obtained using FEM and then compared using measurements.

In Chapter 4, two different wideband energy harvesters are designed. The principle of operation is dependent on the accurate control of resonance frequencies in both the design and manufacturing phases. Actuators were manufactured by two different methods and the measurement results were compared to pinpoint design and manufacturing aspects which affect the dynamical behaviour of the wideband energy harvester. In addition, a model for an energy harvester which harvests energy from walking is developed. The developed model is shown to accurately model the energy output from the piezoelectric energy harvester when it is installed into the sole of a shoe. Also, the dynamics of the energy harvester are examined, as the spring constant in this case is highly nonlinear and the implications of this are further discussed.

The purpose of this work is to provide tools for small signal model creation and show the importance of these models in actuator and energy harvester design. Actuator dynamics can be tuned and evaluated before manufacturing and previously manufactured components can be characterized and their small signal model can be created using methods presented in this work. In energy harvesting, better wideband energy harvesters can be manufactured by using small signal models. The concept of spring constant can also be used in studying the nonlinear behaviour encountered in high displacement shoe mounted piezoelectric energy harvesters.

2 Small signal model parametrization for pre-stressed piezoelectric actuator

2.1 The Butterworth-Van Dyke equivalent circuit

Pre-stressed piezoelectric actuators have not been properly modelled or parameterized before. Multilayer pre-stressed piezoelectric stack actuator was modelled as a simple 2nd degree system and parameterized using step response in [30], but bending pre-stressed actuators have not been properly parameterized. The pre-stressing changes both the mechanical and electrical properties of the actuator [31] and therefore parametrization should be done using measurements. The most commonly used equivalent circuit is the Butterworth-Van Dyke circuit [32] shown in Fig. 1. Other more complicated equivalent circuits have also been developed [33-35], but the classical Butterworth-Van Dyke is the simplest and easiest to implement. It consists of a voltage source V_{in}, the voltage source's output resistance R_{in}, the capacitance C of the piezo component, a transformer with a turn ratio of n, and the mechanical losses which are modelled as r_m. The effective mass of the component is modelled as an inductor with an inductance of m and the spring constant, k, is shown in this circuit as a capacitor. The electrical domain in the left side of the circuit has only the capacitance of the piezo component and the mechanical domain on the right side of the circuit is comprised of an inductor, capacitor and resistor (LCR) circuit which effectively determines the resonance frequency of the component. This is true when the coupling between the electrical domain and the mechanical domain is weak i.e. the transformer ratio is low, which is usually the case in piezoelectric devices.

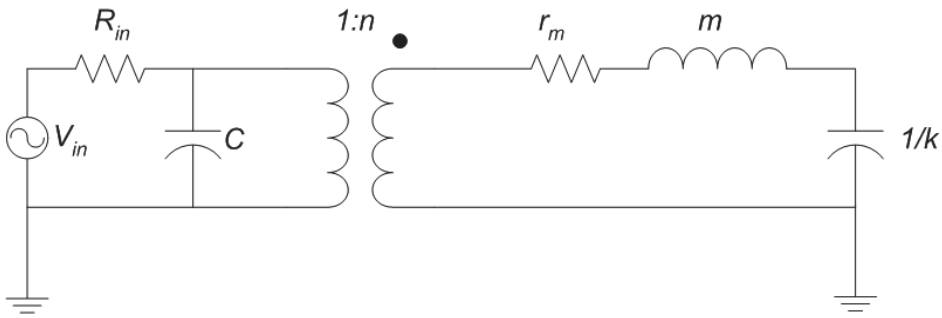

Fig. 1. The classical Butterworth-Van Dyke equivalent circuit for piezoelectric components [Paper I, published by permission of Frami OY].

The resonance frequency, when assuming lossless component i.e. r_m=0, for the circuit in Fig. 1. can be expressed as

$$f_{res} = \frac{1}{2\pi}\sqrt{\frac{k}{m}} \tag{1}$$

and the transformer ratio by

$$n = \frac{F}{V_{in}} \tag{2}$$

where F is the force output of the component under V_{in} excitation. As can be seen, the most obvious method to tune the resonance frequency is to alter the mass of the component by adding mass, m_{added}, to the point of the greatest displacement under vibration. Then the effective mass becomes $m_{eff} = m + m_{added}$.

When current drive is used, for example to reduce the hysteresis of the component, the capacitance of the piezoelectric component couples to the resonating LCR-circuit and the resulting resonance frequency is

$$f_{res} = \frac{1}{2\pi}\sqrt{\frac{k+\frac{n^2}{C}}{m}} \tag{3}$$

As can be seen, the capacitance stiffens the component by adding $\frac{n^2}{C}$ to the spring constant. Thus the new effective spring constant is

$$k_{eff} = k + \frac{n^2}{C} \tag{4}$$

As the spring constant can be altered by the capacitance of the piezoelectric component, the capacitance should be tunable. This, however, still requires the

current drive for the component and in some cases this is not viable. The same capacitance tuning can be obtained with voltage drive by using the circuit shown in Fig. 2. Now a capacitance C_s is connected in series with the actuator and in effect prevents the voltage source from grounding the capacitance of the piezoelectric component.

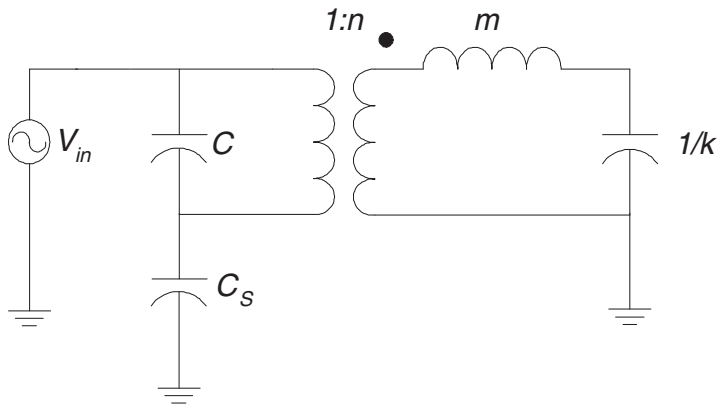

Fig. 2. The equivalent circuit for a piezoelectric actuator with a series capacitor [Paper I, published by permission of Frami OY].

The equation for the resonance frequency is now

$$f_{res} = \frac{1}{2\pi}\sqrt{\frac{k+\frac{n^2}{C_s+C}}{m}} \tag{5}$$

From this equation, it can be seen that the resonance frequency can be tuned between the voltage driven case in equation (1) and current driven case in equation (3). For example, if C_s is 0, the resonance frequency is given by (3) and when C_s >>C, then resonance frequency is obtained by equation (1).

2.2 Experimental development of the equivalent circuit parameters

2.2.1 The design and manufacturing of the test device

The equivalent circuit was developed for a simple pre-stressed unimorph bender, which was clamped from both ends as shown in Fig. 3. The dimensions of the piezoelectric element were 5 x 34 x 0.25 mm. The material was PZT-5H from

Morgan Electro Ceramics Inc. The piezoelectric disc, 35 mm in diameter, was pre-stressed by printing 60 µm Ag-paste on one side and then firing at 850 °C. The coefficient of thermal expansion (CTE) mismatch between the paste and the PZT material created the pre-stress. The details of this process are presented in [36] and [37]. The pre-stressed disc was then cut with a Nd:YVO_4 laser and poled in a 6 MV/m electric field at 100 °C for 30 min. A steel strip with dimensions of 5 x 38 x 0.05 mm was glued on the PZT beam and then fixed to clamps 0.7 mm from the edges of the PZT beam. A mirror was attached to the centre of the beam for subsequent displacement measurements using a Michelson interferometer [38].

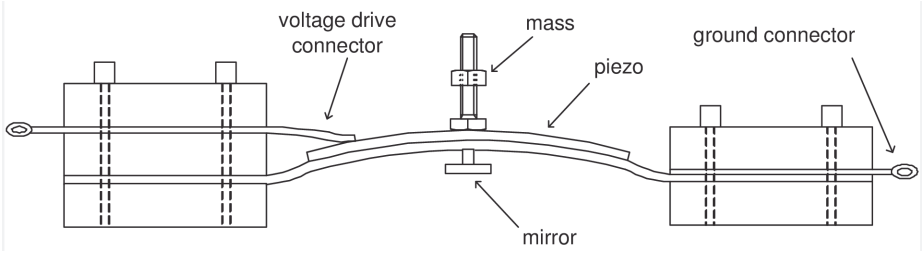

Fig. 3. The pre-stressed unimorph piezoelectric disc clamped from both sides [Paper I, published by permission of Frami OY].

2.2.2 Measurement results and the development of the equivalent circuit model

The measurements consisted of displacement and force measurements. The displacement measurements were done with a Michelson interferometer detailed in [38] and with a signal generator, Agilent 33120A. The force measurements were performed using a Kyowa WGA-650B instrumentation amplifier and a Kyowa LUB-20KB force sensor.

The transformer ratio, n, was obtained using force measurements. The actuator was loaded with 1 N mechanical pre-stress by a force sensor and then actuated with a varying voltage and the change in the force reading recorded. Due to the low sensitivity of the force sensor, relatively high voltages had to be used. Using equation (2) the n together with the error estimate was plotted in Fig. 4. The error estimate was based on the ±0.01 N error of the force reading. The transformer ratio, n, at 200 V was recorded as 2.8 mN/V [Paper I].

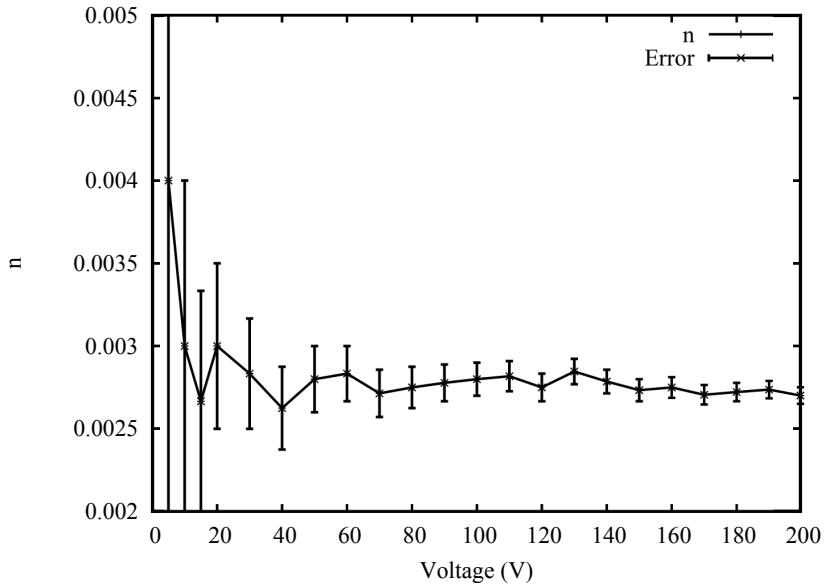

Fig. 4. The transformer ratio *n* and the error estimate versus the input voltage V_{in} [Paper I, published by permission of Frami OY].

A displacement measurement was used to determine the spring constant, k. Under static conditions $k=nV_{in}/x$ and by simply measuring the displacement x under V_{in} excitation using the previously obtained n the k was calculated as 15.6 kN/m [Paper I].

A resonance measurement was used together with equation (1) to determine the effective mass, m_{eff}, which in this case is m, since m_{added} was 0. The resonance was obtained by using displacement measurement and sweeping the frequency. The resulting resonance frequency was found to be 1053 Hz and, using equation (1), the effective mass m_{eff} was obtained as 0.296 g [Paper I].

The capacitance of the piezoelectric component was measured to be 30 nF and if the mechanical losses are omitted i.e. r_m=0, then the equivalent circuit is fully parameterized for studying the effects of added mass and an external capacitor on the resonance frequency. The effect of mass was studied by adding masses i.e. m_{added} in 0.3 g increments, with starting point of 0.779 g i.e. the mass of the bolt.. The resonance frequencies at each mass are shown in Fig. 5 where the calculated values using the small signal parameters and equation (1) are also plotted. As can be seen, the calculated values differed only slightly from the

measured values. The greatest relative error between the calculated and the measured value was 2.5 % at 1.08 g of added mass, as seen in Table 1 [Paper I].

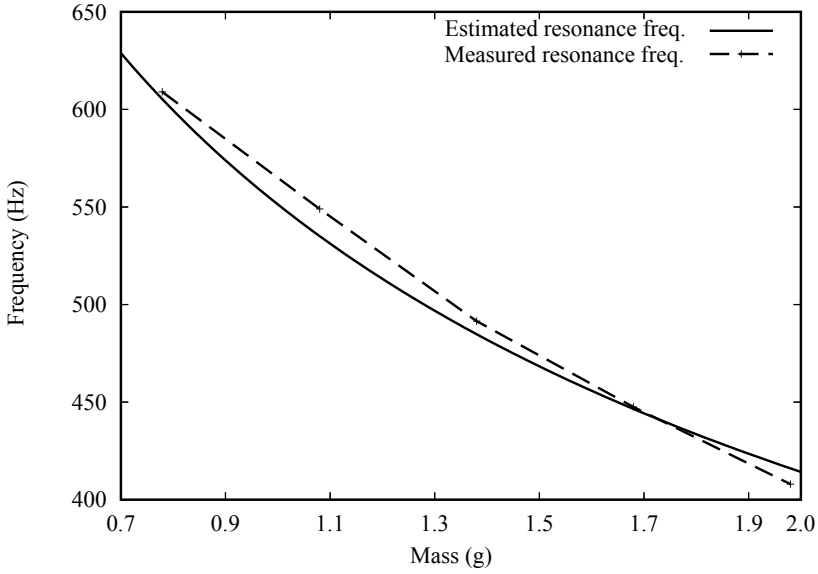

Fig. 5. The resonance frequency versus the added mass of the actuator [Paper I, published by permission of Frami OY].

Table 1. The errors between the measured and the estimated resonance frequencies [Paper I, published by permission of Frami OY].

added mass (g)	0.779	1.08	1.38	1.68	1.98
error (%)	0.6	2.5	1.4	0.3	-1.9

The effect of external capacitance with a simple voltage drive was studied by measuring the resonance frequencies of the prototype and varying the external capacitance, C_s, in the circuit shown in Fig. 2. Four different capacitors were used in the measurements with capacitances 10, 22, 47 and 100 nF respectively and the change in the resonance frequency is shown in Fig. 6 where the analytical results are also shown using equation (5). The prototype had a m_{added} of 0.779 g in the measurements. The error of the frequency measurement was ±0.5 Hz, since the minimum step size for signal generator was 1 Hz, and is shown in Fig. 6 as vertical bars [Paper I]. The measured values closely followed the analytical values

and therefore, taking into account the added mass measurements, the small signal equivalent circuit parameters were successfully obtained.

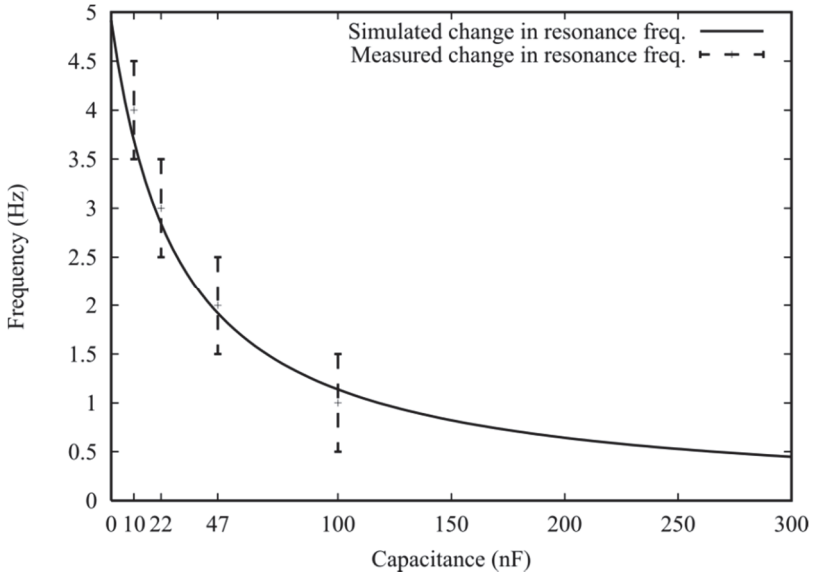

Fig. 6. The change in resonance frequency of the prototype versus the series capacitance [Paper I, published by permission of Frami OY].

A pre-stressed piezoelectric component was manufactured and its small signal model was characterized. When comparing measured and calculated resonance frequencies between the component and its model, a good agreement was found. The model, however, did not incorporate losses, which could therefore affect the obtained simulated results. Nevertheless, as the results show, the absolute error between the component and its model was 2.5 % at maximum and the omission of r_m seems to be a valid decision. The methods provided to parametrize the model can be used in a variety of piezoelectric actuators. Furthermore, the frequency tuning using the model is a useful tool for tuning vibrating piezoelectric components. Series capacitance modulation, i.e. using a tunable capacitor in series with the component, can be used to fine tune the resonance of the component. Energy harvesting applications can benefit from this approach since the frequency can be tuned during operation and thus maintain the optimal harvesting frequency when using high Q-factor harvesters. A high Q-value in energy harvesters is beneficial in terms of obtained energy, but also means that

the energy can only be harvested from a very narrow frequency band. Therefore tunability of components in energy harvesting is an ongoing research endeavor. Mechanical pre-stress devices have been proposed [39], also electrostatic springs with a comb structure [40] and a piezoelectric method [41] where the vibrating beam is bent by a secondary beam to change the shape of the vibrating beam. Electrical tuning methods have been proposed, for example, by adding a shunt capacitance [42] which is similar to the method proposed in this work. The difference is that even with low load impedances the series capacitance can shift the frequency and therefore provide frequency tuning by shielding the electrical side of the small signal model from grounding. This was demonstrated using an inherently low impedance voltage drive on an actuator and recording the change of resonance frequency as shown in Fig. 6. The tunability of the component is naturally dependent of n, as is shown in [43].

3 FPI Actuator design

3.1 FPI mirror actuator

In spectroscopy a Fabry-Perot-interferometer (FPI) may be used to filter desired wavelengths from infrared spectra to determine, for example, the chemical composition of a medicine. Tunability of this interferometer is desirable because the filtered spectrum can then be swept and analyzed. An FPI-filter usually consists of two partially reflecting mirrors with an air gap between the mirrors. The air gap determines the filter frequency and in order to tune this frequency a straightforward approach is to move one or both of the mirrors. Various actuating methods have been used previously such as piezoelectric stack actuators [44-46], thermal actuators [47] and electrostatic actuators [48]. The near infrared channel (NIR) is between 700 – 1000 nm and therefore piezoelectric actuation is well suited for the FPI-filter since the displacement range is ~1 µm which can easily be achieved with piezoelectric materials. The state of the art FPI-filter, of which the author is one of the inventors [46], is shown in [49, 50] where stack-type piezo actuators are installed in the recesses on the side of the mirrors. The drawbacks of the design are the cost of the actuators and the mechanical stresses they introduce to the mirror, which therefore has to be thick in order to provide stiffness to the structure. In this work, the stack actuators are replaced with piezo beams, which results in reduced costs and allows the use of smaller and lighter mirrors. The bending beams, however, can also induce some stresses to the mirror and therefore flexural joints are introduced to enable the use of smaller and thinner mirrors in the filter. The dynamical properties of the FPI-actuator are then examined using both the FEM-method and the small signal method. The aim of the work was to provide a more cost effective alternative to the state of the art actuator with smaller and lighter mirrors.

3.2 The design of the FPI-actuator

The goal of this work was to develop an FPI-filter in a TO-3 package, which meant that the size of the filter was constrained to a diameter of 15 mm with a 3 mm optical aperture. TO-3 package was set as a goal, since it is a standard package used in optical measurement instruments. A three actuator structure was used to provide mirror tilting properties for the filter. This enabled the zeroing of

the manufacturing-introduced optical gap variation, i.e. the mirror tilt. Fig. 7. shows the layout of the filter. The actuators were implemented as beams, as opposed to the stack actuators used previously [44-46]. This reduced the required voltage and provided high displacements in a relatively compact size. The material of the beams was PZ-29 from Ferroperm and the passive layer was Heraeus Heralock 2000 zero shrinkage LTCC tape. This manufacturing process is described in [51-52]. The beams were connected to the mirror holder using a flexural joint. Flexural joints are frequently used in micropositioning stages [53-55] and their design and theory can be obtained from [56-57]. Flexural joints were used to minimize the stress induced in the mirror because stress can bend the mirror and therefore degrade the optical performance of the filter. In cases where the mirror bends, the optical gap between the mirrors varies and therefore the effective aperture changes. The hinges also reduce the stiffness of the beams and therefore increase the displacement of the mirror.

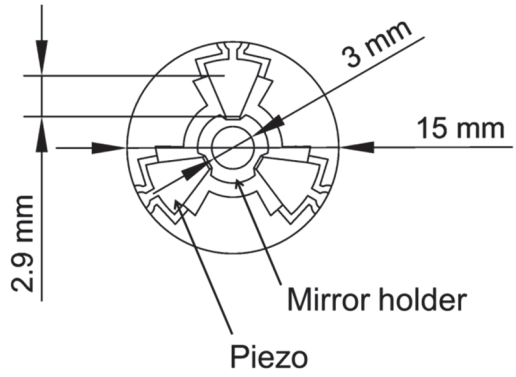

Fig. 7. The FPI-mirror actuator layout.

3.3 The simulation model of the FPI-actuator

The purpose of the modelling of the FPI-actuator was to minimize the stress induced in the partially reflecting mirror attached to the mirror holder. Also, the dynamics of the actuator were of interest because the settling time of a gap adjustment determines the frequency sweep duration. In addition to the simulation of the actuator dynamics, static steady state simulations were carried out in order

to determine the obtainable gap modulation i.e. the displacement of the mirror and the stresses induced in the mirror and the flexural joints.

Comsol Multiphysics software (Comsol Inc., Burlington, MA) was used in the FEM modeling. The model for the FPI-actuator was developed by modelling only the beams and the mirror holder because the supporting rim structure was assumed to be rigid. Therefore the beams were only modelled to have a fixed constraint at the base, since the actuator was glued with cyanoacrylate onto a platform. The active layer was modelled as PZ-29 with the material parameters shown in Table 2, obtained from [58]. The passive layer was modelled as isotropic material with a Young's modulus E of 85 GPa, Poisson's ratio ν of 0.24 and density of 2900 kg/m^3 obtained from [59]. The material properties of the mirror were obtained from [60] with E of 74 GPa and ν of 0.17. The meshed geometry is shown in Fig. 8.

Table 2. The material properties of PZ-29, PZT-5H, steel and plastic cushions, [38,53] [Paper V].

Material	density	$S^E_{11,22}$	$S^E_{12,21}$	$S^E_{13,23,31,32}$	S^E_{33}	$S^E_{44,55}$	S^E_{66}	$d_{31,32}$	d_{33}	$d_{15,24}$	$\varepsilon_{11,12}$	ε_{33}	E	ν
	kg/m^3				$1x10^{-12}$ m^2/N								GPa	
PZ-29	7460	17	-5.78	-8.79	22.9	54.1	45.6	-243	574	724	2440	2870		
PZT-5H	7500	16.5	-4.78	-8.45	20.7	43.5	42.6	-274	593	741	3130	3400		
Steel	7850												200	0.33
Plastic cushion	1150												2	0.4

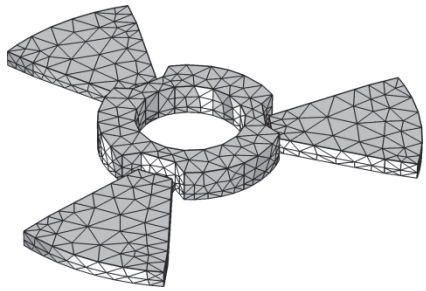

Fig. 8. The meshed geometry of the FPI-actuator [Paper II, published by permission of IEEE].

3.4 The simulation results of the FPI-actuator

The first simulation was a static displacement model where a potential of 100 V was applied to all of the beams. The displacement was recorded from the edge of the mirror holder. The resulting displacement was 1.87 µm. However, the actual measured value was ~1 µm, using OFV-5000 vibrometer (Polytech GmbH, Germany). This error could be explained partly by the poling of the actual component but the bending of the structure could also be a factor since the simulation model omitted the supporting rim structure completely. Some deformation can occur at the base of the beams and was also not included in the model. The same simulation was used to study the stresses induced in the hinges under actuation. The von Mises stress levels were recorded as 37.2 MPa, as shown in Fig. 9. This is still well below the fracture limit of 200 MPa for the LTCC material used [58].

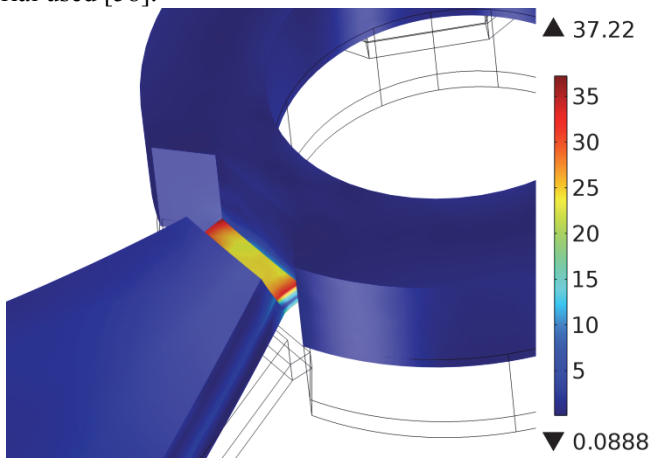

Fig. 9. The von Mises stress (MPa) in the hinge.

The dynamic simulations were done using the eigenfrequency analysis mode on the Comsol Multiphysics software. The first resonance mode was located at 14.7 kHz, whereas the measured resonance was 13.02 kHz. Other resonance modes that were simulated are shown in Fig. 10 [Paper II]. As can be seen, the first resonance is the first mode of a simple beam and the second and the third resonance modes are the tilting resonance modes of the whole structure. The fourth resonance mode is the second bending mode of a beam and it does not include the tilting of the mirror. Analysing these results, it can be deduced that the operating frequencies for this actuator are well below the first resonance of 14.7

kHz. However, some tilting of the mirror was observed at the 21.2 kHz resonance and this has to be taken into account when driving the actuator in continuous operation because mirror tilt could degrade the FPI-operation.

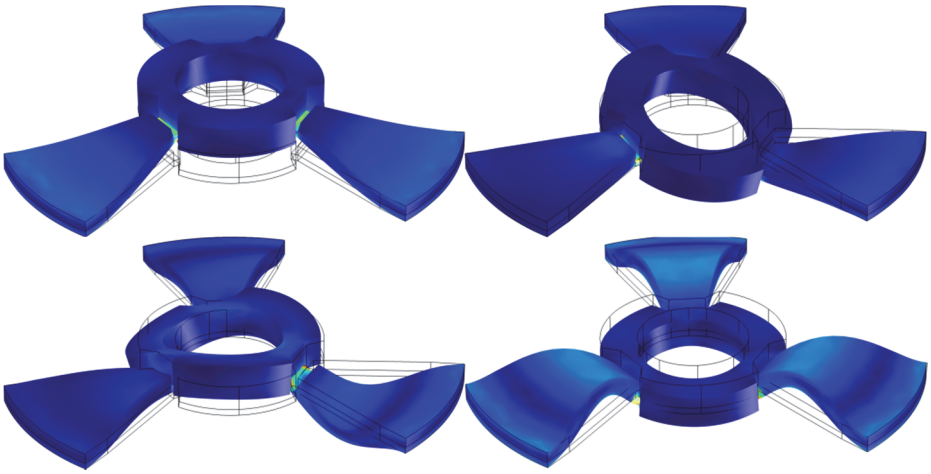

Fig. 10. The first resonance, second, third and fourth resonances at a) 14.7 kHz b) 21.2 kHz c) 71.9 kHz and d) 77.4 kHz respectively [Paper II, published by permission of IEEE].

3.5 The equivalent circuit parameters of the FPI-actuator

The dynamical properties of the FPI-actuator were studied with a mechanical equivalent circuit similar to Fig. 1. In this case, however, only the resonance behaviour was studied and therefore the equivalent circuit was reduced to incorporate only the inertial mass, m, and the spring constant, k. The resonance frequency of this system is stated in equation (1). The total effective mass of the system was $m=m_{eff}+m_m$, where m_{eff} is the effective mass of the moving parts of FPI-module and m_m is the mass of the attached mirror. The parameters for equivalent circuit were obtained by simulating the structure with varying mirror weights. For example if we have two different mirrors with weights m_1 and m_2, the effective mass can be obtained as

$$m_{eff} = \frac{m_2 - \left(\frac{f_1}{f_2}\right)^2 m_1}{\left(\frac{f_1}{f_2}\right)^2 - 1} \quad (6)$$

where f_1 is the resonance frequency with mass m_1 and f_2 is the resonance frequency with mass m_2. The spring constant can be then obtained as

$$k = (2\pi f)^2 m \quad (7)$$

The structure was simulated using a parametric sweep for the mirror density, in order to change the mirror mass. The simulation was carried out as an eigenfrequency simulation to obtain the resonance frequencies. Then using Equation (6), the mean effective mass m_{eff} was obtained as 35.6 mg, using mirror masses ranging from 14 mg to 61 mg. [Paper II]. Now, with the effective mass, m_{eff} , using equation (7), the spring constant, k, was obtained as 326 kN/m [Paper II]. With these values it is now possible to assess the dynamical performance of the FPI-actuator using different sizes and with mirrors of different materials.

3.6 Verification of the equivalent circuit parameters of the FPI-actuator using measurements

The resonance frequency of the prototype was measured both with and without a mirror attached. The attached mirror had a diameter of 4 mm and a thickness of 0.7 mm. The mass of the mirror was 15 mg and thus the density was calculated as 1704 kg/m^3. The measured resonance frequency without the mirror was 13.02 kHz and with the mirror it was 11.31 kHz. Thus the shift in resonance frequency was 13.1 %. The calculated resonance frequencies using m_{eff}, k, and Equation (7), were 14.7 kHz and 12.5 kHz without and with the mirror, respectively. The change in resonance frequency was therefore 15.5 %. As can be seen, the absolute values between the calculated and measured values differed by 12.9 % between the mirror-less cases and by 10.5 % when the mirror was attached. The measured change in resonance frequency after attaching the mirror was 1.71 kHz and the simulated change was 2.2 kHz and 2.4 % in percentage points. However, when the model is applied to the measured case, i.e. using the m_{eff} of 35.6 mg obtained from simulations and calculating the new k using Equation (7), the new k is obtained as 339 kN/m. With this value we can calculate the new resonance frequency with the mirror as 11.4 kHz. The error is only 90 Hz or 0.8 % when compared to the measured value of 11.31 kHz. The reason for the difference between the simulated and measured results can be attributed to slight variations

in geometry and to the fact that the material parameters of both the passive layer and the active layer change when PZT material is sintered together with LTCC [31].

The results demonstrate that by using the equivalent circuit in conjunction with FEM-modelling it is possible to characterize the linearized model, and to use the model as a quick tool for estimating the contribution of the mirror's weight to the resonance frequency of the component. The procedure to do this is first to use FEM-simulations to obtain an average m_{eff} and then calculate the k using the measured resonance frequency of the FPI-actuator without the mirror, and finally, using Equation (7), obtain the resonance frequency with the mirror attached.

An FPI-actuator was developed using beam type actuators instead of stack actuators, which are commonly used in FPI filters. The beam structure was proven to provide the required displacement of 1.87 µm in simulation and a measured value of 1 µm. This was obtained by using flexural hinges to reduce the spring constant and also to minimize the stresses induced in the mirror. The structure differs from state of the art structures by providing a more cost efficient and lighter alternative while having a similar performance. A simple spring mass model was parameterized using FEM-simulations to find the effective mass of the actuator. The model then may be used as a quick tool for estimating frequency shifts when the mass of the mirror is changed. The model also enables the estimation of settling time using standard second order system equations, which is also an important tool in actuator design.

4 Energy harvester designs

In many applications a power source is needed to provide energy for the sensors, data processing and communication. The usual power sources are batteries, accumulators and wired power lines. However, batteries need exchanging, accumulators need recharging and power lines are costly to build and not so convenient in many cases. To tackle these problems various energy harvesting methods have been developed. Energy harvesting can be defined as collecting small amounts of energy from the environment surrounding the component in question. Energy sources typically include solar [61-62], vibration [63], pressure [64-66], magnetic and RF-fields [67-69], chemical [70-71] and temperature [72-74]. Piezoelectric materials are well suited for energy harvesting from vibration and motion in general. Furthermore, the size of piezoelectric harvesters is usually very compact and they are relatively easy to manufacture compared to electrostatic and electromagnetic components.

4.1 Wide band energy harvester

In industrial environments vibration is usually encountered in machinery with rotating parts. This provides a natural source of energy for sensors. When dealing with rotary machinery, however, the majority of the vibration is present at the angular frequencies at which the machines are rotating. This means that the energy harvesters have to be tuned to the same frequency. Piezoelectrical components have a high mechanical Q-value and therefore tuning the resonance frequency can be difficult. For example, to match the rotational frequency of a machine, the narrow bandwidth of the harvester requires a precise match to the machine's frequency. A wideband solution where the Q-value is reduced permits frequency tuning which is much less critical. Also, if the machine has some variation in the rotation speed, the wideband energy harvester is able to continue harvesting the energy provided the frequency of the machine stays within the bandwidth of the harvester. By the same argument, if the source of the vibration is random, a wideband energy harvester is able to harvest more energy compared to a conventional harvester.

Multiple beam wideband piezoelectric energy harvesters include [26,75-76] and also an electromagnetic harvester in [25]. MEMS implementations include a 4 beam SOI structure [77] and a 2 beam micromachined structure [78]. Other methods have been utilized such as coupled resonance structures [79]. Most

recent wideband harvesters use bistable operation, either with magnets [80], buckled beams [81] or springs [82]. These energy harvesters are nonlinear as opposed to multiple beam resonators which are usually linear in behaviour. The multiple beam topology was chosen, because it can provide higher bandwidths by increasing the number of beams. The drawback of this design is its sensitivity to manufacturing tolerances, as will be shown. A method to incorporate manufacturing tolerances into design parameters will be presented in the work. The beam lengths are calculated using a simple recursion instead of the analytical methods presented in [83-84]. The harvesters presented here were manufactured using laser processing as in [26]. A PZT-Steel harvester consisted of a PZT layer glued to a steel layer and a novel PZT-LTCC harvester consisted of a PZT layer and an LTCC layer co-sintered together and then laser cut into shape in order to minimize dimensional errors. This novel technique has not been previously proposed in energy harvesters. The two harvesters are compared with the effect of manufacturing tolerances in mind. The design of the wide band energy harvester
Two different wideband energy harvesters were designed and manufactured. A multiple beam topology was chosen to accomplish the wideband operation. In this beam topology the energy harvester comprises of multiple piezoelectric beams, each with a different resonance frequency

In multiple beam topology, the individual resonance frequency of the *n*:th beam is given as

$$f_{res,n} = \frac{1}{2\pi}\sqrt{\frac{k_n}{m_n}} \tag{8}$$

As the length of the beam is increased, the spring constant, k_n, decreases and the mass, m_n, increases. The absolute values for the spring constant and mass are not needed if only the changes in resonance frequency are required rather than the actual resonance frequencies. Simple relations for the masses and spring constants can be used to accomplish this resonance frequency tailoring. It is known from beam theory that the spring constant of a beam has the relation

$$k_n \propto \frac{1}{l^3} \tag{9}$$

, where *l* is the length of the beam. The mass of the beam has the relation

$$m_n \propto l \tag{10}$$

Substituting these into equation (8), the relation for the resonance frequency is

$$f_{res} \propto \frac{1}{l^2} \tag{11}$$

Now the difference in resonance frequencies between two beams using the beams' damping ratio, ξ, and overlapping factor, α, is generated in this work as

$$f_{res,n} - f_{res,n-1} = \alpha\xi f_{res,n-1} \tag{12}$$

If the overlapping factor is 2, then the relative difference between the beams is exactly the same as the relative bandwidth of the beam, namely 2ξ , which coincides with the half power point in the frequency response. If an energy harvester with beams separated with overlapping factor 2 is made, a flat power spectrum is generated assuming that the power generated by each beam is superimposed. When the overlapping factor is 0, the resonance frequencies are all equal and the total bandwidth of the harvester is the same as that of a single beam, i.e. 2ξ. The power, however, is the total sum of individual beams' power. The ideal value for the overlapping factor is therefore 2 with respect to wide band operation and when using n beams the total bandwidth is $2\xi n$. A more general expression for the bandwidth BW, with the inclusion of the overlapping factor, α, is

$$BW = 2\xi + \alpha\xi(n-1) \tag{13}$$

Now, in order to design the wideband harvester, a recursion based on equations (11) and (12) is developed as

$$l_0 = l_0, l_n = \frac{l_{n-1}}{\sqrt{\alpha\xi+1}} \tag{14}$$

With this equation it is possible to design the resonance frequencies of the beams to satisfy the bandwidth requirements. The starting frequency has to be either calculated or simulated using FEM software to obtain the desired centre frequency. It is also possible to alter the resonance frequency by adding mass to the beams, but in order to taper the resonance frequencies, different masses are required for individual beams.

During manufacturing, different errors are introduced into the dimensions of the beams. The thickness, width and length of the beams can be altered by these errors. For example, the error in beam length can be analyzed as follows. Using equation (12) we get

$$\frac{f_{res,n}}{f_{res,n-1}} = \alpha\xi + 1 \tag{15}$$

And by using equation (11), we get

$$\frac{{l_{n-1}}^2}{{l_n}^2} = \alpha\xi + 1 \tag{16}$$

now if absolute error e is introduced into l_n we get

$$\frac{f_{res,n}}{f_{res,n-1}} = \frac{{l_{n-1}}^2}{(l_n+e)^2} = \frac{{l_{n-1}}^2}{l_n^2+2l_ne+e^2} \sim \frac{{l_{n-1}}^2}{l_n^2(1+\frac{2e}{l_n})} = (\alpha\xi+1)(\frac{1}{1+\frac{2e}{l_n}}) \qquad (17)$$

,where e/l_n is the relative error. This equation shows the effect of error on the resonance frequency shift. To compensate for this we define new overlapping factor α_c which can be obtained by setting

$$(\alpha_c\xi+1) = (\alpha\xi+1)(1+\frac{2e}{l_n}) \qquad (18)$$

and solving for α_c

$$\alpha_c = \frac{1}{\xi}((\alpha\xi+1)\left(1+\frac{2e}{l_n}\right)-1) \qquad (19)$$

where α is the desired overlapping factor. For example, we may set α as 2 and ξ as 0.025 and assume a positive relative error of 0.01 i.e. the actual length of the beam is 1 % longer than the desired length and therefore the resonance frequency is lower than expected. The compensated overlapping factor is obtained as 2.84. This means that the beams are shortened to compensate for the error and the resulting frequency shift is the same as with an overlapping factor of 2 without any error present. In real world cases the error's sign is rarely known *a priori* and therefore a worst case scenario can be analyzed. If the sign of the error is opposite between beams, then $2e$ can be used as a value for the error. In this case, if the overlapping factor is chosen as 2, the worst case scenario widens the gap between the two resonances in such a way that the ripple exceeds the 3dB limit. For example, if we have a 1 % error in the length of the beams, we can use -2 % as the relative error (2 % shorter beam than anticipated) with an overlapping factor 2 and ξ again as 0.025. Using equation (19) we get the compensated overlapping factor as 0.32, which differs greatly from the original overlapping factor of 2. This demonstrates the high sensitivity of the frequency tuning of multibeam energy harvesters.

In this case, only the error in the length of the beam was analyzed, but by using beam equations, the errors for width and thickness can also be analysed using similar methods to those presented here.

4.1.1 PZT-steel wideband energy harvester

A five beam energy harvester was designed and manufactured. A circular closed shape was chosen in order to facilitate encapsulation of the component. The outline of the harvester is shown in Fig. 11.

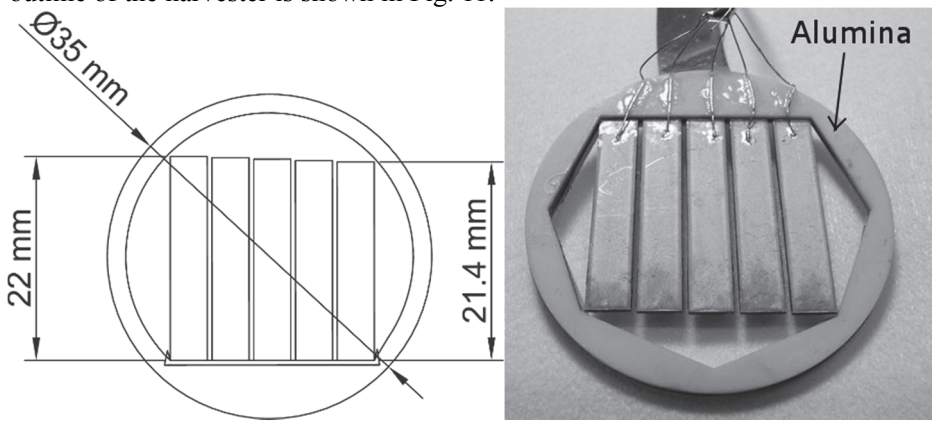

Fig. 11. a) The dimensions and b) the manufactured prototype [Paper III, published by permission of Suomen Automaatioseura].

The active material for the prototype was PZT-5H from Morgan Electroceramics. The material parameters can be seen in [85]. The passive layer was steel and the thicknesses of the active and passive layers were 375 µm and 150 µm respectively. The length of the first beam was chosen as 22 mm, in order to fit as long beams as possible inside the 35 mm piezo disc with sufficient support area. The width of the beam was also maximised to 4 mm in order to improve the power output of individual beams. It is important to maximize the beam length in order to reduce the resonance frequency of the harvester because the natural frequency is high for beams of this size. When the base frequency of the harvester is made as low as possible, it is easier to reduce it further to the desired level by adding mass at the tip of the beams. The design parameters for calculating the length of the beams were 0.025 for the damping ratio, ξ, and 0.5 for the overlapping factor, α. Damping ratio was chosen using *a priori* experience of vibrating piezoelectric beams. A low value for the overlapping factor was chosen in order to ensure proper overlapping and therefore higher power output at the expense of the bandwidth, since hand gluing and placement generate higher tolerances. These tolerances could be estimated as 100 µm for placement, but glue thickness was not estimated, but could have been measured using a series of

cross-sectional cuts. The resulting beam lengths were 22, 21.9, 21.7, 21.6 and 21.4 mm.

4.1.2 LTCC wideband energy harvester

In addition to the traditional PZT-steel unimorph wideband energy harvester a PZT-LTCC monomorph structure was also manufactured in order to test whether the more precise monolithic process improved the frequency performance of a wideband harvester. The active material of the harvester was PZ29 (Ferroperm A/S, Denmark) instead of the PZT-5H used for the PZT-steel harvester. The passive material was Heraeus Heralock 2000 LTCC tape. The main difference between the previous prototype and the LTCC embedded prototype was in the manufacturing of the layered structures. In the previous prototype each layer was cut with a laser and then glued together. The gluing, which was done by hand, added errors in the positioning of the layers in the XY-plane and also in the Z-direction as the glue layer thickness was not precisely controlled. In the LTCC prototype, however, the positioning was done using a jig and the layers were sintered together so that a glue layer with arbitrary thickness was not present. The prototype is shown in Fig. 12.

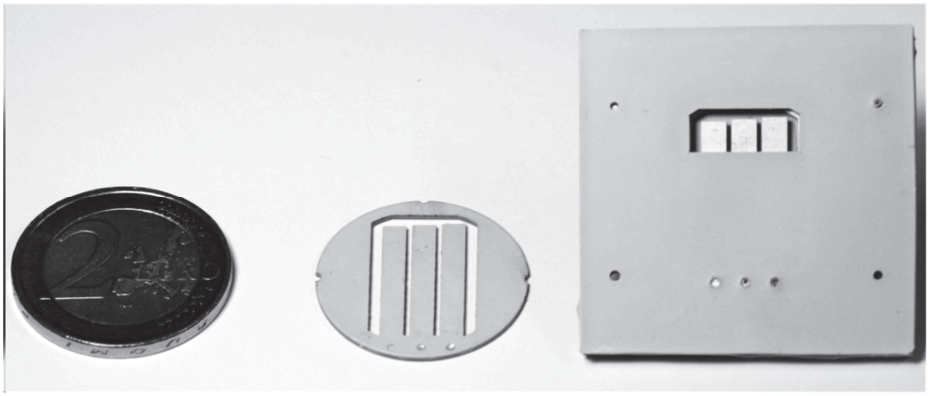

Fig. 12. The PZT-LTCC harvester without (middle) and with lid (right) [Paper IV, published by permission of Elsevier Ltd].

The harvester was designed with three beams instead of five as in the PZT-steel prototype. The beam lengths were calculated using equation (14) and using the starting length of 18 mm, the overlapping factor, α, of 1 and the damping factor, ξ,

of 0.025. Higher overlapping factor for this harvester was chosen as much higher dimensional accuracy was expected for the monolithic structure. This resulted in a length series 18, 17.78 and 17.56 mm. Beam width was 3 mm and the layer thicknesses were 375 and 270 μm for the PZT and LTCC layers, respectively. The difference between the beam lengths was 220 μm and for the PZT-steel prototype it was 150 μm. The larger overlapping factor eased the manufacturing of the harvester since the required length difference was greater than with a smaller value of α. This is important in structures where the beam lengths are restricted as in this case where the 25 mm disc diameter restricts the beam length compared to the previous PZT-steel prototype where a 35 mm disc was used. Smaller disc diameter was used because of material availability and better manufacturability of the smaller disc.

4.1.3 Measurement results and comparison between the harvesters

The wide band energy harvesters were measured both as an actuator and a harvester. The actuator measurements were done using a vibrometer OFV-5000 (Polytech GmbH, Germany) for the displacement measurements. A piezo stack Piezomechanik Pst 150/7/160 VS12 was used to generate the desired acceleration for the energy harvesting measurements. The energy harvesting electronics are shown in Fig. 13 where a common rectifier is used together with a capacitor (1 μF) as the energy storage unite unit.

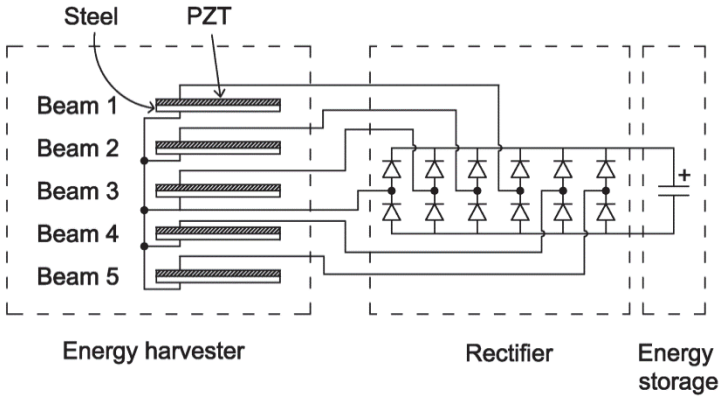

Fig. 13. The schematic of the energy harvesting electronics [Paper III published by permission of Suomen Automaatioseura].

Actuator measurements were performed in order to assess the resonance frequencies of the beams. Fig. 14 shows the frequency response curve of the PZT-steel harvester under 10 V_{p-p} excitation. It can be observed that beam number 5 was not working, thus making the energy harvester effectively a 4 beam harvester. Furthermore, the order of the resonances was 1-2-4-3 as opposed to the designed order of 1-2-3-4. Fortunately this does not weaken the performance since the spacing of the resonances is still acceptable. Beams number 4 and 5 were located side by side and since the amplitude of beam number 4 was also attenuated as in the case of beam 5, it can be said that same problem could be affecting for both beams. This can be for example the glue layer between the steel and PZT, which by altering the total thickness locally changes the resonance frequency of the beams located in the said area. The resonance frequencies for the beams 1, 2, 3 and 4 were 695, 700, 724 and 712 Hz, respectively [Paper III]. According to equation (12), resonances 695, 703.7, 712.5 and 721.4 Hz were obtained. When comparing this series with the measured values, errors for the measured and calculated frequencies were obtained as 0.5 %, 1.6 % and -1.3 %. The first calculated frequency was assumed to be 695 Hz and the error was therefore 0 %. As can be seen, the relative errors in the frequencies were small but could still result in the beams switching places in the frequency domain. In this prototype the resonance frequencies for beams 3 and 4 were very close to the designed values as they have switched places, but this was not according to design. The displacement amplitudes of the resonances were similar for beams 1, 2 and 3, but beam 4 was attenuated to roughly half of the other beams' displacement.

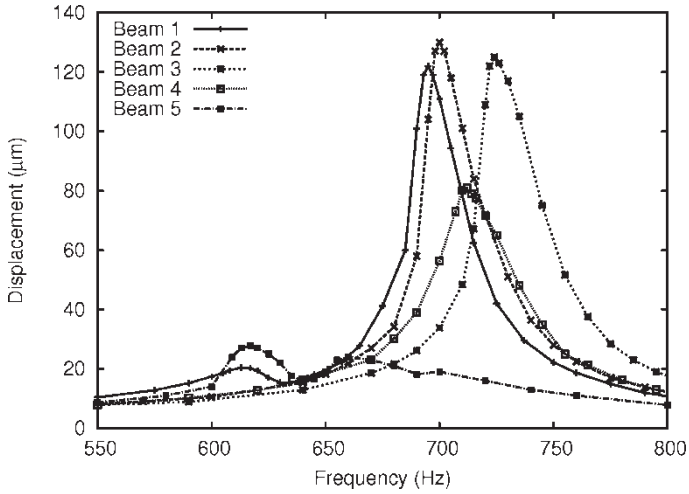

Fig. 14. The Frequency response of the PZT-steel energy harvester under 10 $V_{p\text{-}p}$ sinusoidal actuation [Paper III published by permission of Suomen Automaatioseura].

Similar measurements were performed for the PZT-LTCC prototype and the resulting frequency response curve is shown in Fig. 15. As can be seen, the order of the resonances was as desired 1-2-3 and the respective resonance frequencies were 1109, 1137 and 1155 Hz [Paper IV]. The calculated values using equation (12) were 1100, 1137 and 1165 Hz. Therefore the errors were 0.82, 0 and 0.86 % for the frequencies. Thus, the errors were essentially half of those of the PZT-steel prototype. Further insight into the effect of the overlapping factor is gained when the frequency differences are studied. The differences fres,n-fres,n-1 for the PZT-steel model were 5, 24, -12 Hz. The calculated values, however, were 8.7, 8.8 and 8.9 Hz. Now the errors for the differences were 74 %, 172 % and 234 %. These values differ greatly from the absolute errors which were at maximum 1.6 %. The same measured differences for the PZT-LTCC prototype were 28 and 18 Hz and the calculated values were 37 and 28 Hz. Now the errors are 24 and 36 %. As the required frequency difference is larger due to the overlapping factor α, the relative error also becomes lower. Therefore larger overlapping factors should be used even though the power output is somewhat reduced because this ensures that wideband operation is maintained even though errors are introduced in the manufacturing process. This can however result in bandpass ripple exceeding the 3 dB level and if that is not acceptable, then lower overlapping factor should be used. This is a design choice that should be considered when

facing high manufacturing tolerances. When comparing the magnitudes of the resonances between Figs. 14 and 15, it can be noted that for the PZT-LTCC prototype the magnitudes are in descending order, which is characteristic of beam resonances in actuation.

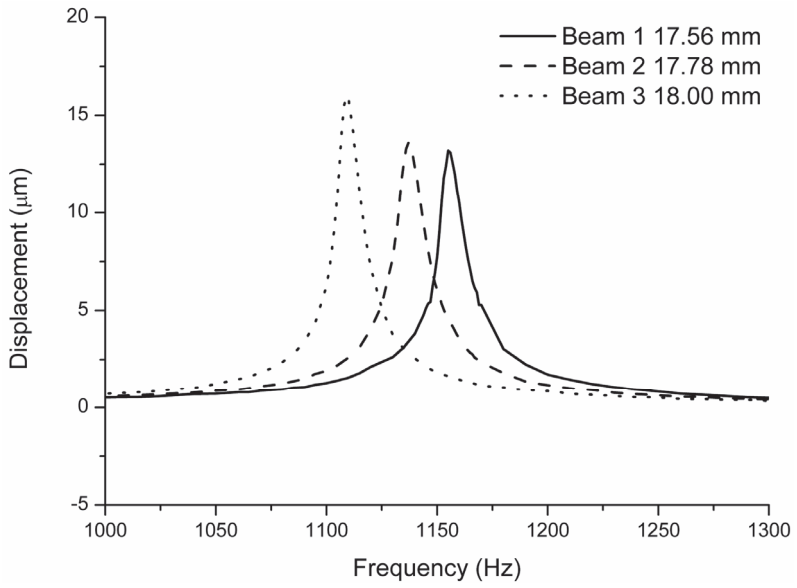

Fig. 15. The PZT-LTCC harvester under 1 V_{p-p} sinusoidal actuation [Paper IV, published by permission of Elsevier Ltd].

The wideband operation of the harvesters was measured using a frequency sweep and connecting the harvester into the circuit shown in Fig. 13. In this measurement, the harvester was attached to a shaker and the frequency of the shaker was varied while the amplitude remained constant. For the PZT-steel prototype a 6 μm peak-to-peak displacement was used for the actuation. With constant displacement, the acceleration amplitude ranged from 36 to 76 m/s^2as the frequency was swept from 550 to 800 Hz. The voltage of the capacitor was recorded and the energy content of the capacitor was then calculated from the voltage. The resulting frequency response is shown in Fig. 16. The centre frequency was 717 Hz, with a 3 dB bandwidth of 54 Hz [Paper III]. The improvement of the bandwidth when comparing it to a single beam, with the designed Q-value of 20, is 50 %. Using measured Q-value of 24.6, the

improvement was 85 %. For the PZT-LTCC prototype the frequency response is shown in Fig. 17. In this measurement, the amplitude was 1 µm, as the frequency was higher than in the PZT-steel case. This resulted in accelerations between 20 and 33 m/s^2. The centre frequency was 1147 Hz and the bandwidth was 62 Hz [Paper IV]. Therefore the actual improvement in the bandwidth compared to a single beam was 5.4 times larger i.e. 540 % since the single beam's measured bandwidth was 11 Hz. The measured Q-value of the single beam was 103 on average and the value used in the design phase was 20. In comparison, the PZT-steel prototype had an average Q-value of 24.6 which deviated only 23 % from the value used in the calculations. The high Q-value of the PZT-LTCC prototype is also seen in the Fig. 17 as the pass-band of the harvester had a considerable ripple which should not exist with such a low overlapping factor. For the PZT-steel prototype the pass-band notch was not due to a high Q-value, because the Q-value was close to that of the value used in the calculations, but rather due to the low output of beam number 4, evident in Fig. 14.

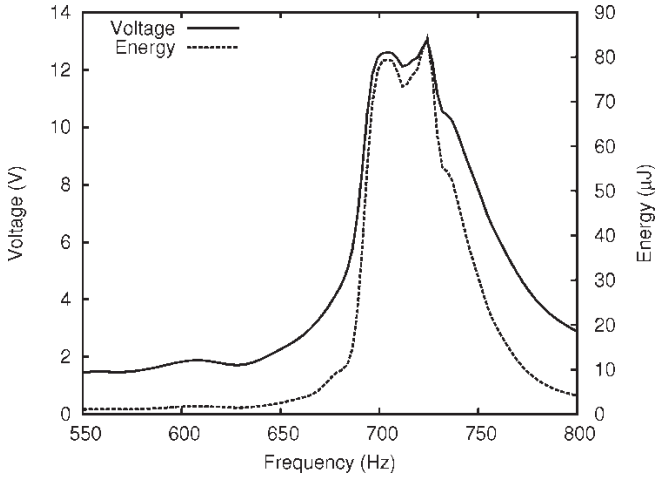

Fig. 16. The buildup voltage and energy of the capacitor on PZT-steel energy harvester [Paper III published by permission of Suomen Automaatioseura].

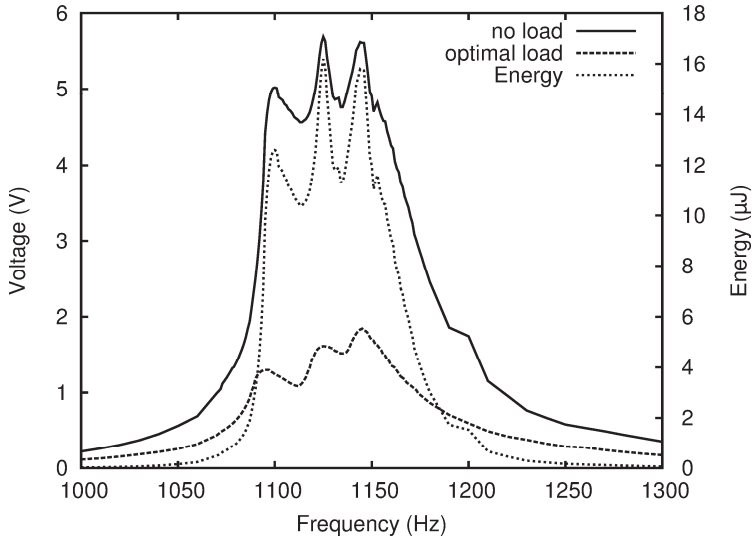

Fig. 17. The buildup voltage of the capacitor of the PZT-LTCC harvester, the voltage across the optimal load resistance and the energy of the capacitor.

As the PZT-LTCC prototype showed, the Q-value can differ greatly from design to design. This affects the resonance frequency placement and if the error in the Q-value estimation is large, the pass-band of the energy harvester will generate ripple. Another important design decision is the choice of manufacturing process. As was shown, the less precise manufacturing process where layers were glued by hand in the PZT-steel prototype led to large errors in the resonance frequencies of the beams. In contrast, the LTCC process proved to be very good in manufacturing precise geometries and therefore the resonance frequencies of the beams were very close to the designed values. The third important aspect is the choice of the overlapping factor as it can to some extent alleviate the tolerances in manufacturing, especially when using a large number of beams. This is of course at the expense of bandwidth and energy, since a higher overlapping factor increases the bandwidth but decreases the power and by using a lower overlapping factor the effect is the opposite. The error analysis showed the high sensitivity of length variations to the resonance frequency, and this can be used as a design tool in the selection of manufacturing process and overlapping factor. The performance of the harvesters could be improved by introducing mass at the tip of the beams, because that lowers the resonance frequencies and also improves the power output of the energy harvester [86]. In this work, masses were not

introduced, because the focus was on the frequency tuning by length variation of beams and other variables were kept to a minimum.

The small signal analysis proved to be a useful tool when designing wideband multibeam harvesters, since together with simple beam equations, process tolerances and material Q-value information it could be used in designing the beam resonance frequencies which fulfilled the specified frequency range properties. In [26] a similar laser processed structure was developed and the claimed improvement of the bandwidth was 200 % compared to that of a single beam for a 6 beam structure and 33 % per beam. The results were 50 % and 540 % for the PZT-steel harvester and PZT-LTCC harvester, respectively. Improvements per beam were 12.5 % and 180 %. A MEMS implementation in [77] claimed resonance frequencies between 237 – 244.5 Hz with four beams, which roughly translates to a relative bandwidth of 3.12 %, whereas the PZT-steel prototype and the PZT-LTCC prototype obtained 7.5 % and 5.4 %, respectively. Besides performance enhancements, the PZT-LTCC prototype provides an integrated package for the harvester and also enables the integration of harvesting- and sensor electronics into the harvester itself. This then enables very robust harvesters for environmentally demanding applications, since LTCC is both a circuit board and a package at the same time.

4.2 Modelling energy harvesters for walking

Wearable electronics have been developed to be used, for example, in firefighters' outfits and in military attires. Various sensors embedded in shoes, gloves and other wearable items need power, and batteries or accumulators are usually used. However, the problem with these is the weight and the need to recharge or replace them. Energy harvesting is a natural solution for wearable electronics. A wide range of solutions exist for generating power from the movement of the body such as harvesting the heel strike of the shoe [87], the pressure of the foot [88], the movement of the knee joint [89], the straps of the backpack [90] and the heat from the body[91]. In this work, however, the pressure and heel strike of the foot were used as the energy source. Energy harvesting from walking presents many challenges. The low operation frequency of ~ 1 Hz limits the use of resonating structures and therefore the coupling of energy from the mechanical domain into the electrical domain in piezoelectric materials. Also, the harvester should not hinder the movement or provide discomfort to the user of the device. The energy density of the harvester device should also be maximized since the space

available is limited. Furthermore, when embedding energy harvesters into shoes, the force experienced by the harvester is not a simple step function, but rather has a defined shape, which affects the power output and also the FEM modelling of the device.

In this chapter, the performance of a cymbal harvester is studied using FEM-modelling. The mechanical input into the harvester is measured and the results are used as an input to the FEM simulator. The mechanical input in this case is the force experienced by the harvester when mounted inside the sole of a shoe during walking. FEM modelling provides a tool for understanding the behaviour of the piezo electric harvester under high stresses during walking. The harvester in question is a cymbal type transducer, which is typically used as an actuator [92-93]. FEM modelling is a commonly used tool in cymbal [93-98], and also in harvester design. Sinusoidal excitation was used in [99-100] with a relatively high excitation frequency of 100 Hz. The power output of simple piezoelectric discs was studied in [101]. FEM and analytical methods was used in [102], to study the effect of an additional steel layer attached to the piezoelectric layer in a cymbal configuration. In [103], circumferential slots were incorporated into the endcaps of the cymbal and FEM together with analytical methods was used as a tool. However, the accurate simulation of cymbals subjected to the actual walk profile has not previously been studied. The incorporation of arbitrary waveforms, nonlinear mechanics and large displacements into a single cymbal energy harvester simulation is a novel approach which gives valuable information about cymbal energy harvesters under high load conditions.

4.2.1 The design of the shoe mounted energy harvester

The shoe mounted piezoelectric harvester was designed to be embedded into the sole of the shoe. Furthermore, the purpose of the study was to create a FEM-model of the cymbal structure and to model the energy generation from walking. Since the force experienced by the harvester is not sinusoidal, a transient model with a relevant force profile is needed. Also, energy harvesting simulations require the combination of both the mechanical and electrical domain simulations. This model addresses all these requirements. The basis of the cymbal structure was a PZT-5H disc 35 mm in diameter into which brass connector rings were glued together with convex steel endcaps. The endcaps were pressed into shape using a mould. This process was done manually and therefore the endcap shape was not entirely uniform. The cymbal and its dimensions are shown in Fig. 18.

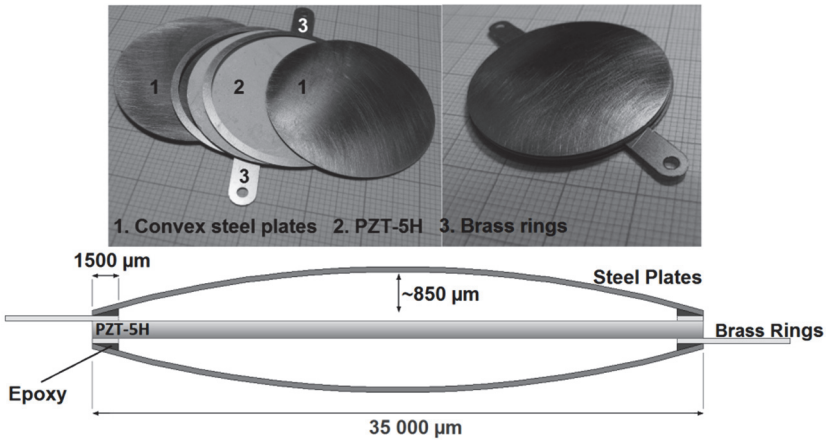

Fig. 18. The cymbal structure and the individual parts of the shoe mounted piezoelectric harvester [Paper V, published by permission of SAGE publishing].

4.2.2 The FEM model of the energy harvester

The profile of the endcap was measured using a micrometer screw gauge and one half of the profile was used in the model by mirroring it into the axial geometry. This introduced some errors into the model since the endcap geometry was not modelled in all quarters of the actual geometry. The measured profile is shown in Fig. 19.

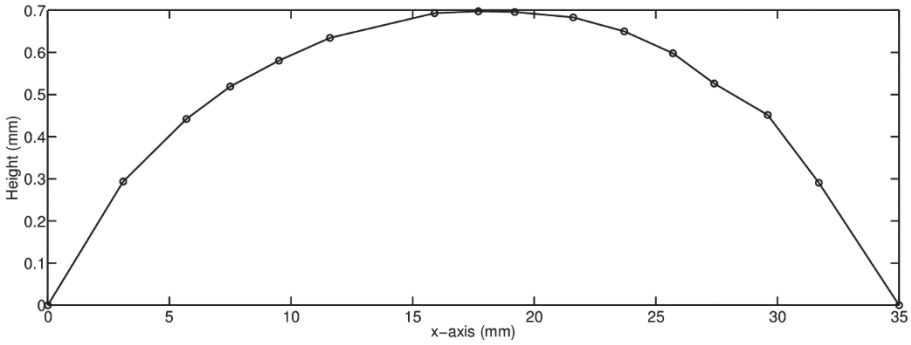

Fig. 19. The measured profile of the endcap used in model and measurements [Paper V, published by permission of SAGE publishing].

The geometry of the model was designed to be parametric where all of the geometric properties were added as variables that could be modified during simulation passes. The shape of the endcap was modelled as a normalized shape vector ranging from 0 to 1. The concavity and radius together with other geometric parameters defined the actual points of the endcap. This design provided a powerful tool for optimizing cymbal designs as in [22]. The meshed geometry of the axial-symmetric design is shown in Fig. 20 together with plastic cushions at the top and bottom of the cymbal. The plastic cushions were incorporated into the model because the cymbal was installed into a plastic holder which was then installed into a shoe sole. The force of the heel pressure was therefore conveyed into the cymbal through these plastic cushions in a controlled manner. The measurement system is presented in detail in Paper V.

The material parameters for the piezoelectric material, steel and the plastic cushions are shown in Table 2. These values were obtained from the manufacturer's catalog [85] for the PZT. The steel's and nylon plastic cushion's values were obtained directly from the Comsol software (Comsol Multiphysics 4.2 a). As can be seen from Fig. 20, triangular elements were used. The order of the elements was quadratic and therefore the accuracy of the simulations was adequate compared, for example, to constant strain triangle (CST) elements which cannot properly calculate the stresses inside the triangle. Furthermore, the geometric nonlinearities setting was applied for the simulations. This setting is also known as the large deformation setting in some other FEM softwares. This is necessary because the deformation levels are large in the simulations; the applied stroke for the cymbal in the simulations was 1.5 mm, which is near the point where the endcap touches the piezo disc.

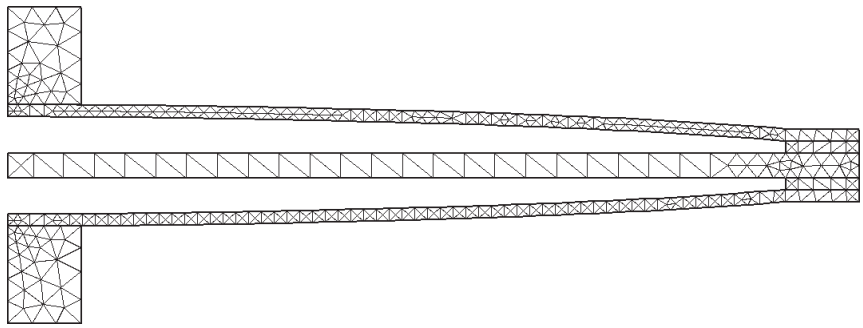

Fig. 20. The meshed axial-symmetric geometry of the cymbal [Paper V, published by permission of SAGE publishing].

The lower plastic pad was fixed from the bottom as a fixed boundary condition and the top pad was in turn actuated with the input force. The force experienced by the harvester was measured from the prototype during actual walking. This force waveform was then used as an input for the top pad as a force type boundary condition in the transient simulations. The force measurement data was filtered to remove high frequency content in order to increase the step size in simulations and therefore shorten the total simulation time. This filtered force profile is shown in Fig. 21. As the results show, the pace of walking was roughly 1 Hz. This is also shown by [104-106] to be a good average pace for walking.

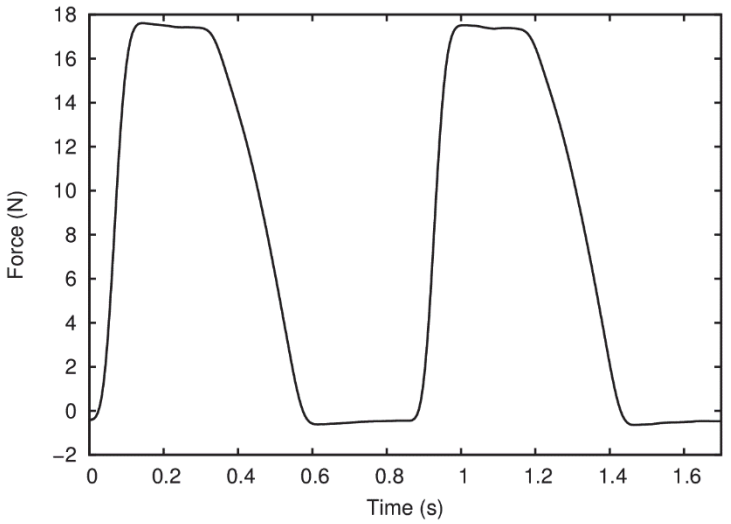

Fig. 21. The force input for the shoe mounted energy harvester at 0.5 mm stroke [Paper V, published by permission of SAGE publishing].

The electrical boundary conditions were set as ground for the bottom electrode of the PZT disc and the top electrode was set as a terminal connection for an external SPICE circuit which consisted of a simple load resistor. This external circuit was simulated concurrently with the FEM simulations using the same Comsol software. The SPICE simulations provided an easy method for calculating the power dissipated by the external load resistor. Furthermore, the optimal load resistance was easily obtained using parametric simulations where the resistance was swept.

4.2.3 The simulation results of the energy harvester

The first simulation was carried out as a static displacement *vs.* force simulation where the stroke was applied to the top pad of the energy harvester and the resulting force on the same surface was recorded, as shown in Fig. 22. The same curve was also generated by measuring the prototype and these results are also shown in the figure. As can be seen, the simulated values largely agreed with the measured values although some differences appeared. Namely, in the area between 0.6 to 1.6 mm the simulated forces were below the measured values and also the nonlinearity was greater in the simulated curve than in the measured one. The maximum error occurred at 1.1 mm with 8.8 % error. It has to be noted also that the most significant contributors to this displacement *vs.* force curve were the endcaps of the component, because the material of the piezoelectric disc deforms very little compared to that of the endcaps. Therefore the mechanical properties of the endcaps will have the most effect on the total performance of the harvester, as will be shown later. The simulation type can also explain the difference between measured and simulated results, since the model of the endcap was only one half of an endcap mirrored to generate an axial symmetric geometry. From Fig. 22, the average spring constants for the measured and simulated cases were obtained as 34.1 kN/m and 30.4 kN/m, respectively. As the nonlinearity of the curve is quite strong a more general nonlinear temporal spring constant can be obtained by first fitting a curve for the force *vs.* displacement curve. The force in the case of the simulated model is

$$F(d) = 2.014 \cdot 10^{10} d^3 - 4.114 \cdot 10^7 d^2 + 4.0808 \cdot 10^4 d + 1.497 \quad (20)$$

, where d is the displacement of the endcaps and the F is the reactive force on the pad. The temporal spring constant is by definition the derivative of F with respect to d as

$$k(d) = \frac{\partial F}{\partial d} = 6.042 \cdot 10^{10} d^2 - 8.228 \cdot 10^7 d + 4.0808 \cdot 10^4 \quad (21)$$

This function reaches its minimum of 12.8 kN/m at 0.68 mm and its maximum of 63.7 kN/m at 1.6 mm when the displacement is restricted to 0.4 to 1.6 mm as in the measurements. As Fig. 23 shows, the spring constant is highly nonlinear, especially in the modelled case.

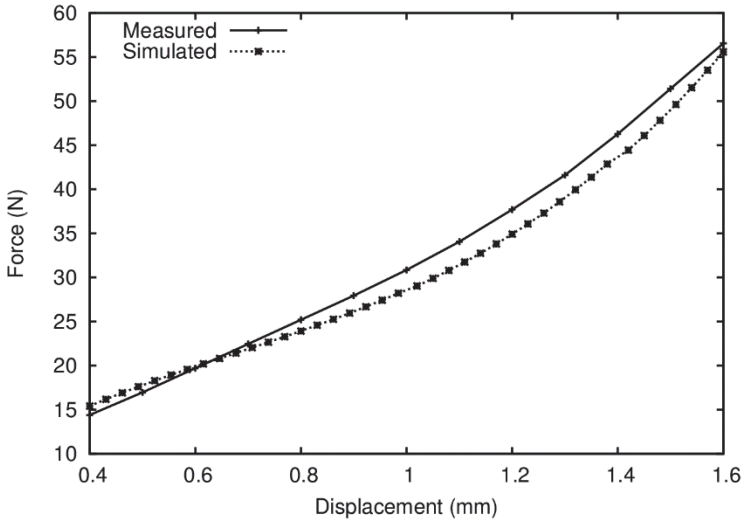

Fig. 22. The displacement vs. force of the cymbal actuator [Paper V, published by permission of SAGE publishing].

For the measured harvester the force as a function of displacement was

$$F(d) = 1.137 \cdot 10^{10} d^3 - 2.122 \cdot 10^7 d^2 + 3.955 \cdot 10^4 d + 1.194 \quad (22)$$

and the spring constant

$$k(d) = 3.411 \cdot 10^{10} d^2 - 4.244 \cdot 10^7 d + 3.955 \cdot 10^4 \quad (23)$$

The minimum spring constant was located at 0.62 mm with a value of 26.4 kN/m. The maximum at 1.6 mm resulted in 59 kN/m. When comparing the simulated and measured spring constants, the measured spring constant had a higher minimum and slightly lower maximum, therefore the simulated spring constant exhibited a higher nonlinearity compared to the measured case. The minimum occurred roughly at the same displacement. Furthermore, when comparing the maximum deviation from the average spring constant obtained from the linear fitting, the simulated case deviated 33.3 kN/m and the measured case deviated 24.9 kN/m. This shows that the average spring constant cannot be used in cases where large deformations are encountered such as in a cymbal under high loads. The spring constants in equations (21) and (23) are plotted in Fig. 23.

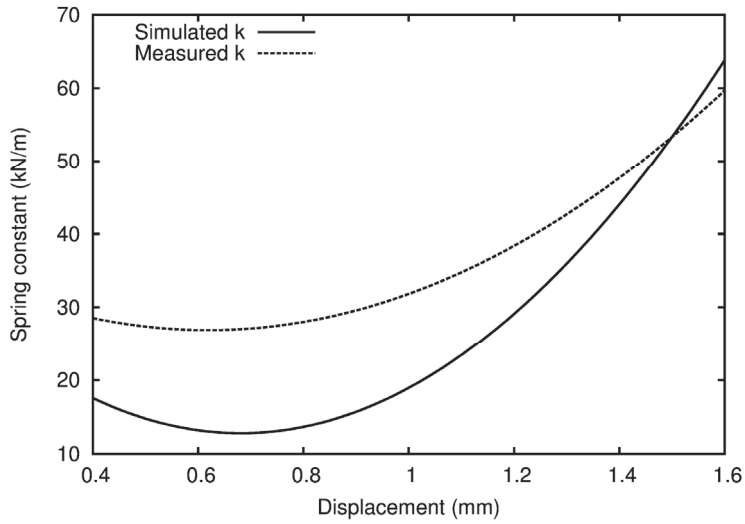

Fig. 23. The spring constant versus displacement of the measured and simulated end cap of the shoe mounted piezoelectric harvester.

The force applied to the top of the end cap is transformed by the end cap into radial stress in the piezoelectric disc. This transformation was simulated with a similar simulation as in Fig. 22, where the force versus displacement was modelled. In this case, however, the force was used as an input and the displacement of the end cap and the von Mises stress inside the piezoelectric disc was simulated. These results are shown in Fig. 24. As can be seen, at 30 N the stress induced into the piezo disc started to drop. When comparing figures 23 and 24, it can be seen that the spring constant started to rise after 0.8 mm and at the same displacement the change in stress growth in Fig. 24 started to decrease. Therefore the drop in stress relaying properties of the end cap can indeed be attributed to the nonlinear spring constant. Deformations of the end cap under different loads are shown in Fig. 25. As can be seen, the deformations are noticeable and at 30 N a recess had formed in the middle of the end cap. This deformation therefore stiffened the structure giving rise to the highly nonlinear spring constant shown in Fig. 23.

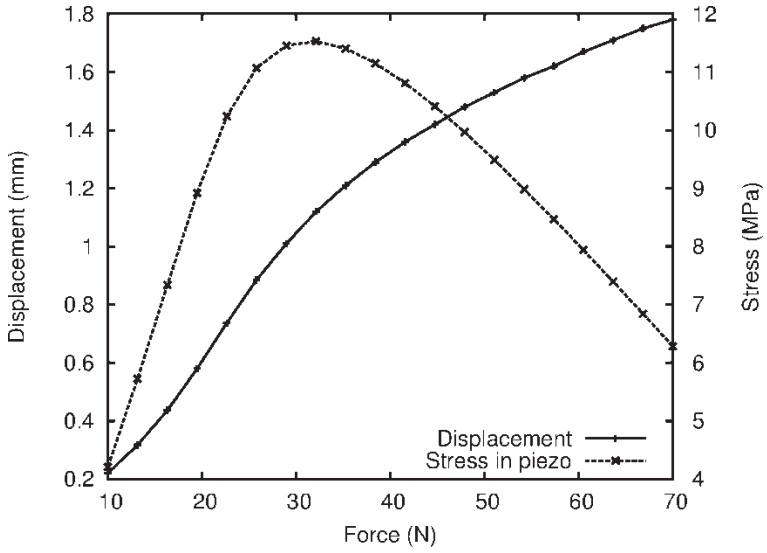

Fig. 24. Displacement and piezo stress as a function of force of the cymbal harvester [Paper V, published by permission of SAGE publishing].

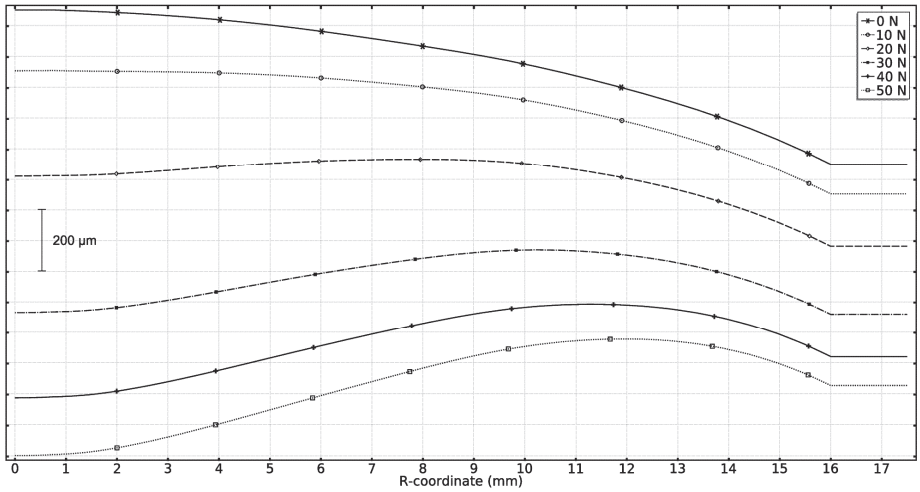

Fig. 25. The end cap shape under different loads [Paper V, published by permission of SAGE publishing].

The power generation simulations were done using the force profile in Fig. 21. The simulation was carried out as a transient simulation with the force applied to

the top pad. A similar sine signal was also used for comparison, with a peak-to-peak value adjusted to match the walk profile. The results are shown in Fig. 26.

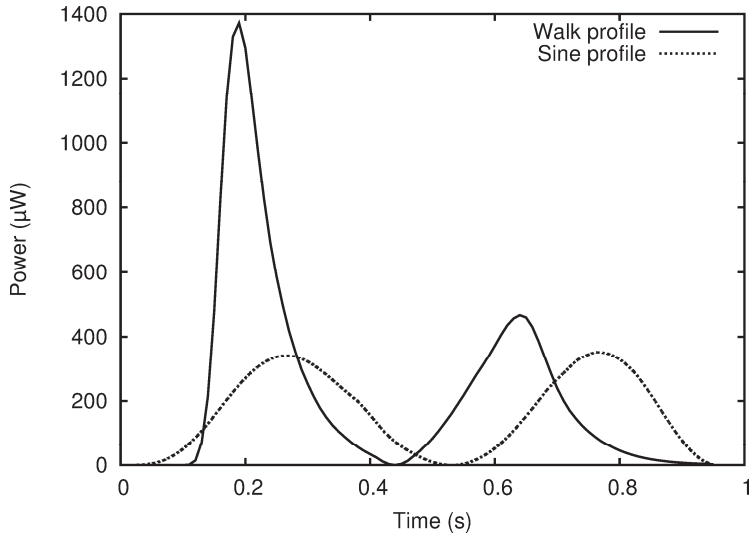

Fig. 26. The power generation with the walk and sine force profile under 17 N peak load with optimal 2.63 MΩ load resistance [Paper V, published by permission of SAGE publishing].

The load resistance was adjusted to 2.63 MΩ which was measured to be the optimal resistance [Paper V]. The optimal resistance was also simulated using transient simulation with the walk profile. In that case the optimal resistance was 3.0 MΩ which is very close to the measured value and therefore the use of the measured value is also justified in the simulations. These results are shown in Fig. 27. As can be seen in Fig. 26, the walk profile produced a large peak when the heel compressed the cymbal. When the heel was in the static pressure mode as seen in Figs. 21 and 26 during 0.2 to 0.4 seconds, the power decays to zero and when the heel rises and the cymbal experiences decompression the power rises again to produce a similar peak but only smaller. When comparing the walk profile with the sine profile, it can be seen that the compression cycle produced roughly a 4.5 times higher peak compared to the sine profile [Paper V]. The decompression cycle, however, produced a similar peak to the sine peak. The compression cycle's rise time was 60 ms and in the decompression cycle it was 184 ms. The shorter rise time explains the higher power output during the compression cycle and also why the sine signal produced such a low power

output. The difference in power levels is also seen in Fig. 27, where the walk profile produced ~100 µW more power in the 2.63 MΩ load resistor, which is 167 % higher power generation compared to sine signal. This result emphasizes the importance of correct input signal modelling in energy harvesting simulations where the input signal deviates from a sine signal.

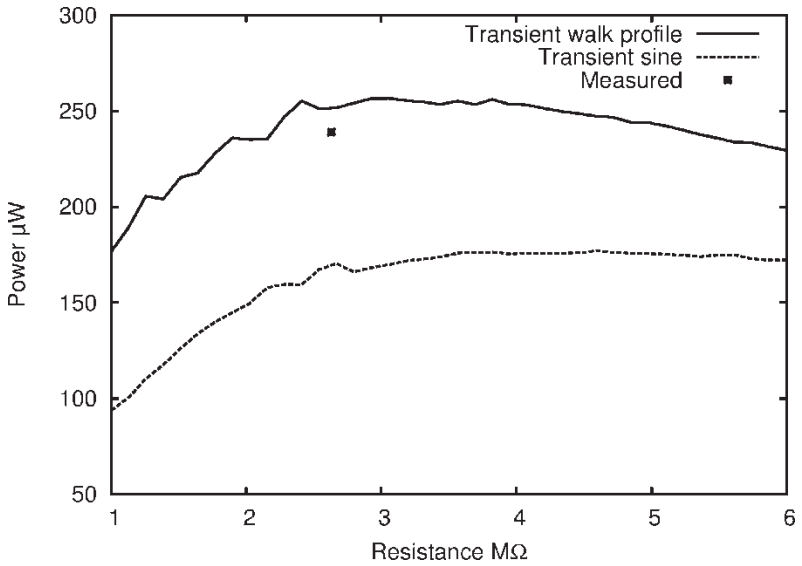

Fig. 27. The power vs load resistance of the walk and sine input [Paper V, published by permission of SAGE publishing].

The average power generations were measured using 12 different stroke values ranging from 0.5 mm to 1.6 mm. The same displacements were also used in simulations. In these simulations the profile in Fig. 21 was scaled to match the force profile at the given stroke. The load resistance was adjusted to 2.63 MΩ in both the measurements and simulations. Both results are shown in Fig. 28, where the average power versus stroke distance is shown. The simulations were carried out as transient simulations as in the case of the simulations depicted in Fig. 27 and the average power was calculated from one walk cycle and the result was plotted. As can be seen from Fig. 28, the simulated values agree well with the measured values up to 1.2 mm displacements. At 1 mm displacement, the measurements show a deviation, which is probably caused by a measurement error. The power output for the simulated model peaked at 1.3 mm with 640 µW. The measured power peaked at 1.5 mm with 780 µW. The error between the

simulated and measured power below 1.3 mm was 7.1 % with the exception of 1 mm displacement where the error was 14.7 %. Above 1.3 mm the simulated and measured values diverged and the simulated values saturated. As discussed earlier, the saturation derives from the nonlinear spring constant of the end caps. The same saturation did not occur until 1.5 mm displacement in the case of the measured values. Fig. 23 shows that the measured spring constant exhibited considerably greater linearity compared to the simulated case. This can also explain the different saturation behaviour of the measured cymbal compared to the simulated model. Therefore, when generating a model for a cymbal energy harvester, a comparison between the spring constants is encouraged in order to gain insight into establishing reliable models for energy harvesting simulations with high deformations.

As the results showed, the developed model accurately modelled the behaviour of the cymbal piezoelectric harvester. The accurate input signal and geometry modelling, together with the combination of mechanical and electrical simulations, generated a useful tool for cymbal type energy harvester design. This model can be extrapolated into other topologies and operational environments and thus provides added value to large stroke energy harvester designs.

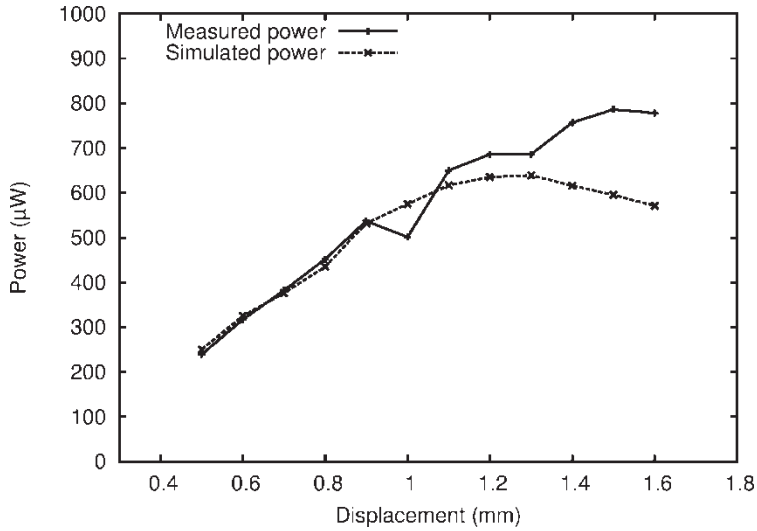

Fig. 28. The average measured and simulated power versus displacement of the cymbal harvester [Paper V, published by permission of SAGE publishing].

5 Conclusions

The main scope of this thesis was to develop methods to combine the equivalent circuit analysis and finite element methods to improve the design process of actuator and energy harvester dynamics. In addition, a new FPI structure was developed to provide more cost effective alternative to the state of the art FPI actuator. FEM analysis also provided further insight of the cymbal energy harvester under large displacements during walking. The small signal parameters were obtained either from measurements or from the FEM model. The small signal model of the component could then be used in estimating resonance frequencies of beams either in FPI actuators or wideband energy harvesters. In addition, the nonlinear spring constant of a cymbal energy harvester was discussed and its effect on the saturation behaviour was investigated in relation to stroke displacement or input force.

The Butterworth-Van-Dyke equivalent circuit was developed for a pre-stressed piezoelectric actuator. The small signal parameters were obtained from a series of measurements. The model was tested against the component with resonance measurements with varied added masses. The model deviated only 2.5 % at maximum. As the equivalent circuit reveals, the series capacitance can be used in tuning the resonance frequency of the actuator. This was tested both with the actual component and the small signal model and the calculated results deviated only 14 % from the measured values. It was also noted, that by adding a series capacitor into the piezoelectric component, the internal capacitance is decoupled from the input/output impedance of the external electronics. This provides a method to tune the resonance frequency of the energy harvester by electrical means in low load impedance situations.

An FPI actuator was designed and simulated with PZ-29 as the active material and LTCC as the passive material. The design featured a flexural hinged mirror holder which alleviated stress in the mirror. This stress can bend the mirror and therefore degrade FPI performance by affecting the local gap length. The stress levels were also studied in the hinge area made of LTCC material and they were confirmed to be well below the fracture limit. The reduction of stress levels induced into the mirror enables the use of thinner and lighter mirrors which then improves the transient properties of the FPI-actuator. In this work, the dynamical parameters, namely the spring constant, k, and the effective mass, m_{eff}, of the actuator were obtained using simulations. Eigenfrequency simulations were carried out with a series of added masses. Resulting resonance frequencies were

then used in calculating the effective mass, m_{eff}, and the spring constant. The small signal model was then compared to measurements where a mass was added to the mirror holder. The resonance frequencies between the model and the actual component differed only 0.8 % when mirror was attached, thus validating the small signal approach. The results also showed that a small TO-3 sized FPI-actuator can be made with beam structure instead of the state-of-the-art stack actuators.

Two different types of wideband energy harvesters were designed to collect energy from a vibrating environment and one cymbal type energy harvester to collect energy from walking. A conventional PZT-Steel energy harvester was developed and characterized. This harvester contained five differently tuned beams, with the purpose of generating a series of resonances that are tuned in a controlled manner to provide the wideband operation. The resonance frequencies were tuned by controlling the beam length and thus the effective mass and the spring constant of the beam. This approach proved effective as the difference between the measured and calculated resonance frequencies was 1.6 % at maximum, although two beams had switched places when put into order of their resonances.

The second wideband harvester was a PZT-LTCC energy harvester which had only three beams. This manufacturing process was more controlled because the layers were stacked using a jig instead of manual alignment as in the PZT-Steel case. The beams were tuned similarly to the PZT-Steel case apart from the overlapping factor, α, which was 1 instead of 0.5 for the PZT-Steel case. The results showed that the resonance frequencies differed only 0.86 % from the calculated values which is nearly two times better than the PZT-Steel case. The resulting frequency response of the energy harvester, however, exhibited ripple which was an indicator of an incorrect damping factor, i.e. Q-value, assumption. Surprisingly, the actual Q-value of the beam was five times that of the designed value. This manifested itself as a pass-band ripple for the energy harvester. Nevertheless, the PZT-Steel prototype did not suffer from this, since the designed and measured Q-values were close. This proved that the overlapping factor and Q-value have to be carefully decided and measured in the design process. In addition, the manufacturing process has a very large influence on the resonance frequencies, because the tolerances of the process can affect the geometry of the component and therefore the resonance frequency. This was shown by an error analysis, where the error on the beam length was studied. A method was developed to incorporate this error into the overlapping parameter selection.

Small signal modelling when used in conjunction with correct Q-values, can be used to tailor the bandwidth of multibeam harvesters. The design parameters have to be selected according to manufacturing tolerances to optimize the bandwidth. This was demonstrated using two different manufacturing processes and the results gave valuable information about the tailoring of the design parameters.

The energy harvester for walking was developed using a cymbal harvester. The shape of the endcaps was measured and these results were then input into the FEM model. As the harvester was designed to be embedded into the sole of a shoe, the actual force profile of walking was measured and again inputted into the model. This enabled FEM simulations with a high accuracy in simulating the power levels obtained from walking. The almost completely parameterized model provides a powerful tool for further optimizing cymbal type energy harvesters. The model was first verified by carrying out a force *vs.* displacement simulation as well as a similar measurement with the actual prototype. The results differed by only 8.8 %, which was caused largely by the difference in the endcaps' spring constant. The spring constants were compared between the simulated and the measured cases and the simulation model exhibited larger nonlinearity compared to the measured component. This proved that the endcap modelling differed from the actual component. However, as the power generation simulations and measurements were carried out, the simulated model followed closely the values of the measured component up to 1.3 mm displacement. After that the model started to saturate. The measured component exhibited similar saturation, but at larger displacements. Again, the stiffening of the structure was found to be the cause of this behaviour. The endcaps' ability to transfer input force into radial stress in the piezoelectric disc showed a maximum at around 30 N after which the stress started to drop and therefore the output energy of the piezoelectric component saturated. This was a result of the stiffening of the endcaps under high loads. The presented simulation tool provides a powerful method for optimizing the endcap geometry to combat the stiffening encountered in this work.

This work presented methods to combine finite element techniques and small signal analysis to improve the design process of actuator and energy harvester dynamics. The small signal parameter, k, was also used in explaining the saturation behaviour of the cymbal energy harvester, where it was found to be nonlinear. This work presented novel methods to tailor the bandwidth of wideband energy harvesters according to manufacturing tolerances and material properties, namely Q-factor. The simulation model of a cymbal type energy

harvester used in a high stroke energy harvesting environment is a novel contribution to energy harvesting. This work also proved that the accurate modelling of the input signal together with time based transient modelling is an essential part of high stroke simulations. The generated model is also expandable to other types of energy harvesters and the methods developed can be used in a variety of different energy harvesting simulations and harvester development.

References

1. Subaru telescope (2013). URI: http://www.subarutelescope.org. Cited 2013/12/12.
2. Juuti J, Leinonen M & Jantunen H (2008) Piezoelectric and Acoustic Materials for Transducer Applications : chapter Micropositioning editori:Ahmad Safari & E. Koray Akdogan: 319–340.
3. PI (2001) Micropositioning, nanopositioning, nanoautomation solutions for cutting-edge technologies. PI catalog.
4. Li M, Yuan J, Guan D & Chen W (2011) Application of piezoelectric fiber composite actuator to aircraft wing for aerodynamic performance improvement. Science China Technological Sciences. 54(2): 395–402.
5. Suleman A & Costa AP (2004) Adaptive control of an aeroelastic flight vehicle using piezoelectric actuators. Computers & Structures 82(17-19): 1303–14.
6. Giessibl FJ (2003) Advances in atomic force microscopy. Rev Mod Phys 75(3): 949–982.
7. Veeco Intruments Inc (2003) SPM Training Notebook 004-130-00 Revision E.
8. Veeco Instruments Inc (2004) Dimension 3100 Manual Revision D.
9. Ang WT, Garmón A, Khosla PK & Riviere CN (2003) Modeling rate-dependent hysteresis in piezoelectric actuators. In: Proc 2003 IEEE/RSJ International Conference on Intelligent Robots and Systems, IEEE, Piscataway, USA: 1975–1980.
10. Comstock RH (1981) Charge control of piezoelectric actuators to reduce hysteresis effects. U.S. Patent 4,263,527.
11. Ronkanen, P. Kallio, P & Koivo, H.N (2002) Current Control of Piezoelectric Actuators with Power Loss Compensation. IEEE/RSJ International Conference on Intelligent Robots and Systems (IROS), Lausanne, Switzerland, October pp. 1948–1953.
12. Åström KJ & Wittenmark B (2008) Adaptive Control:Second Edition, Dover Books.
13. Ru CH, Sun L & Kong MX (2005) Adaptive inverse control for piezoelectric actuator based on hysteresis model. In: Proc 4th International Conference on Machine Learning and Cybernetics, IEEE, Piscataway, USA: 3189–3193.
14. Sun L, Ru C & Rong W (2004) Hysteresis compensation for piezoelectric actuator based on adaptive inverse control. In: Proc 5th World Congress on Intelligent Control and Automation, IEEE, Piscataway, USA: 5036–5039.
15. Dinulovic D & Gatzen HH (2006) Microfabricated inductive micropositioning sensor for measurement of a linear movement. IEEE Sens J 6 (6): 1482–1487.
16. Furuta A, Munekata M & Higuchi T (2002) Precise positioning stage driven by multilayer piezo actuator using strain gauge. Jpn J Appl Phys 41: 6283–6286.
17. Harb S, Smith ST & Chetwynd DG (1992) Subnanometer behavior of a capacitive feedback, piezoelectric displacement actuator. Rev Sci Instrum 63 (2): 1680–1689.
18. Sacconi A, Picotto GB & Pasin W (1999) The IMGC calibration setup for microdisplacement actuators. IEEE Trans Instrum Meas 48(2): 483–487.
19. Leinonen M, Juuti J & Jantunen H (2007) Interface circuit for resistive sensors utilizing digital potentiometers. Sensors and Actuators A:Physical. 138(1): 97–104.

20. Ferrari, A & Mittica, A (2012) FEM modeling of the piezoelectric driving system in the design of direct-acting diesel injectors. Applied Energy 99: 471–83.
21. Mehlfeldt, D, Weckenmann, H & Stohr G (2008) Modeling of piezoelectrically actuated fuel injectors. Mechatronics 18: 264–72.
22. Poikselkä K, Leinonen M, Palosaari J, Vallivaara I, Haverinen J, Röning J & Juuti J (2015) End cap profile optimisation of piezoelectric Cymbal actuator for quasistatic operation by genetic algorithm, Journal of Intelligent Material Systems and Structures, published online 2015/1/14, DOI: 10.1177/1045389X14566526.
23. Van Dyke, K.S (1928) The Piezo-Electric Resonator and Its Equivalent Network. Proceedings of the Institute of Radio Engineers 16(6): 742–764.
24. Wurpts, W & Twiefel, J (2012) Analysis of ultrasonic vibro-impact systems with equivalent circuits and the harmonic balance method. Sensors and Actuators A 200: 114–22.
25. Sari I, Balkan T & Kulah H (2008) An electromagnetic micro power generator for wideband environmental vibrations. Sensors and Actuators A 145-146: 405–13.
26. Rguiti, M Hajjaji, A D'Astorg, S Courtois, C & Leriche, A (2013) Elaboration and characterization of a low frequency and wideband piezoceramic generator for energy harvesting. Optical Materials 36(1): 8–12.
27. Xue, H Hu, Y & Wang, Q-M (2008) Broadband piezoelectric energy harvesting devices using multiple bimorphs with different operating frequencies. IEEE Trans. Ultrason.,Ferroelectr. Freq. Control 55: 2104–8.
28. Shahruz, S M (2006) Design of mechanical band-pass filters for energy scavenging. J. Sound Vib. 292: 987–98.
29. Ferrari, M Ferrari, V Guizzetti, M Marioli, D & Taroni, A (2008) Piezoelectric multifrequency energy converter for power harvesting in autonomous microsystems. SensorsActuators A 142: 329–35.
30. Hunstig, M & Hemsel T (2010) Parameter Identification and Model Validation for the Piezoelectric Actuator in an Inertia Motor. Journal of the Korean Physical Society 57(4): 952–4.
40. Palosaari J, Juuti J, Heinonen E, Moilanen P & Jantunen H (2009) Electromechanical Performance of Structurally Graded Monolithic Piezoelectric Actuator. Journal of Electroceramics 22(1): 156–162.
41. Berlincourt DA, Curran DR & Jaffe H (1964) Piezoelectric and Piezomagnetic Materials and Their Function in Transducers. in W.P. Mason ed., Physical Acoustics, Academic, NY, 1(A): 169–270.
42. Ballato A & Ballato J (1995) Modern Piezoceramic Equivalent Networks. Ultrasonics Symposium, Proc. IEEE 1: 683–686.
43. Adriaens JMTA, Koning WL & Banning R (1997) Design and Modelling of a Piezo-actuated positioning mechanism. Decision and Control, Proc. of the 36th IEEE Conference on. 2: 1978–1983.
44. Goldfarb M & Celanovic N (1997) Modeling piezoelectric stack actuators for control of micromanipulation. IEEE Contr. Syst. Mag. 17: 69–79.

45. Juuti J, Jantunen H, Moilanen VP & Leppävuori S (2005) Poling conditions of pre-stressed piezoelectric actuators and their displacement. Journal of Electroceramics 15: 57–64.
46. Juuti J, Jantunen H, Moilanen VP & Leppävuori S (2006) Manufacturing of Pre-stressed Piezoelectric Actuators by Post-fired Biasing Layer. IEEE Transactions on Ultrasonics, Ferroelectrics, and Frequency control 53(5): 838–46.
47. Moilanen H & Leppävuori S (2001) Laser Interferometric Measurements of Displacement-field Characteristics of Piezoelectric Actuators and Actuator Materials. Sensors and Actuators A 92: 236–334.
48. Eichhorn, C Goldschmidtboeing, F & Woias, P (2008) A frequency tunable piezoelectric energy converter based on a cantilever beam. Proc. PowerMEMS 2008+ microEMS2008 (9–12 November 2008, Sendai, Japan) 309–12.
49. Lee, K B Lin L & Cho, Y H (2008) A closed-form approach for frequency tunable comb resonators with curved finger contour. Sensors Actuators A 141: 523–9
50. Peters, C Maurath, D Schock, W & Manoli, Y (2008) Novel electrically tunable mechanical resonator for energy harvesting. Proc. PowerMEMS 2008+ microEMS2008, (Sendai, Japan, 9–12 November 2008) 253–6.
51. Muriuki, M. G. (2004) An Investigation into the Design and Control of Tunable Piezoelectric Resonators. Ph.D. Dissertation, University of Pittsburgh, PA.
52. Shu, Y. C Lien, I. C Wu, W. J (2007) An Improved analysis of the SSHI interface in piezoelectric energy harvesting. Smart Materials and Structures 16: 2253–64
53. Reay N, Ring J & Seaddan R (1974) A tunable Fabry–perot filter for the visible. J. Phys. E Sci. Instrum. 7(8): 673–677.
54. Atherton P & Reay N (1981) A narrow gap, servo-controlled tunable Fabry–perot filter for astronomy. Mon. Not. R. Astron. Soc. 197: 507–511.
55. Ollila J, Juuti J, Leinonen M & Saari H (2008) FI20085947 Fabry-Perot interferometer and method for its manufacture. Finnish patent.
56. Yu B, Pickrell G, Woong KJ & Wang A (2004) Thermally tunable extrinsic Fabry–perot filter for white-light interferometry. Frontiers in Optics.
57. Patterson J (1997) Micro-mechanical voltage tunable Fabry–perot filters formed in (111) silicon. Nasa Langley Research Center, Hampton, WV, nasa technical paper 3702.
58. Saari, H Aallos, V-V Akujärvi, A & Antila, T (2009) Novel miniaturized hyperspectral sensor for UAV and space applications. Proc. SPIE7474, Sensors, Systems, and Next-Generation Satellites XIII.
59. Mäkeläinen, A Saari, H Hippi, I Sarkeala J & Soukkamäki, J (2013) 2D Hyperspectral Frame Imager Camera Data in Photogrammetric Mosaicking. International Archives of the Photogrammetry, Remote Sensing and Spatial Information Sciences XL-1/W2: 263–7.
60. Heinonen E, Juuti J & Jantunen H (2007) Characteristics of piezoelectric cantilevers embedded in LTCC. J. Eur. Ceram. Soc. 27(13–15): 4135–4138.

61. Sobocinski M, Zwierz R, Juuti J, Jantunen H & Golonka L (2010) Electrical and electromechanical characteristics of LTCC embedded piezoelectric bulk actuators. Adv. Appl. Ceramics 109(3): 135–138.
62. Zhang Z & Hu H (2009) Flexural Mechanism Design Analysis for a New Piezoelectric Inchworm Actuator. Measuring technology and mechatronics automation, ICMTMA '09 International conference on 1: 98–101.
63. Furukawa E, Mizuno M & Doi T (1995) Development of a flexure-hinged translation mechanism driven by two piezoelectric stacks. JSME International Journal, Series C: Dynamics, Control, Robotics, Design and Manufacturing 34(4): 743–748.
64. Yang R, Jouaneh M & Schweizer R (1996) Design and characterisation of a low-profile micropositioning stage. Precision Engineering 18: 20–29.
65. Paros JM & Weisbord L (1965) How to design flexure hinges. Machine Design 37: 151–156.
66. Lobontiu N (2003) Compliant Mechanisms: Design of Flexure Hinges. CRC Press.
67. Data matrix from ferroperm website URI: http://www.ferroperm-piezo.com/ Cited 2013/12/10.
68. Roellig M, Schubert L, Lieske U, Boehme B, Frankenstein B & Meyendorf N (2010) FEM assisted development of a SHM-piezo-package for damage evaluation in airplane components. in 11th. Int. Conf. Thermal. Mechanical and Multiphysics Simulation and Experiments in Micro-Electronics and Micro-Systems (EuroSimE): 1–9.
69. Shin-Etsu Chemical Co. Material datasheet URI: http://www.shinetsu.co.jp/en/products/pdf/garasu.pdf Cited 2013/10/12.
70. Green MA (2004) Third generation photovoltaics: advanced solar energy conversion. Springer Verlag.
71. Randall JF (2005) Designing indoor solar products. John Wiley & Sons.
72. Beeby SP, Tudor MJ & White NM (2006) Energy harvesting vibration sources for microsystems applications. Measurement Science & Technology 17: 175–195.
73. Cunefare, K.A Skow, E.A Erturk, A Savor, J Verma, N & Cacan M.R (2013) Energy harvesting from hydraulic pressure flunctuations. Smart Materials and Structures 22(2): 25–36.
74. Pfenninger, A Vogel, R Koch, V.M & Jonsson M (2014) Performance Analysis of a Miniature Turbine Generator for Intracorporeal Energy Harvesting. Artificial Organs 38(5): 68–81.
75. Deterre, M Lefeuvre, E & Dufour-Gergam, E (2012) An active piezoelectric energy extraction method for pressure energy harvesting. Smart Materials and Structures 21(8)
76. Mi, M Mickle, M.H Capelli, C & Swift, H (2005) RF Energy Harvesting with Multiple Antennas in the Same Space. IEEE Antennas and Propagation Magazine 47(5):100–6.
77. Moghe, R Divan, D & Lambert, F (2011) Powering Low-Cost Utility Sensors using Energy Harvesting. Proc. of the 2011-14th European Conference on Power Electronics and Application (EPE 2011) : 1–10.

78. Vo, M.N & Noras, M.A (2013) Energy Harvesting from Electromagnetic Field Surrounding A Current Carrying Conductor. Proc. ESA Annual Meeting on Electrostatics 2013: 1–12.
79. Brogioli D (2009) Extracting renewable energy from a salinity difference using a capacitor. Phys. Rev. Lett. 103 058501–1–4.
80. Guo, W Cao, L Xia, J Nie, F-Q Ma, W Xue, J Song,Y Zhu, D Wang, Y & Jian L (2010) Energy Harvesting with Single-Ion Selective Nanopores: A Concentration – Gradient-Driven Nanofluidic Power Source. Advanced Functional Materials 20(8):1339–44.
81. Leonov V, Fiorini P, Sedky S, Torfs T & Van Hoof C (2005) Thermoelectric MEMS generators as a power supply for a body area network. In: Proceedings of the 13th int conf on solid–state sensors, actuators and microsystems, transducers 2005: 291–294.
82. Kishi, M Nemoto, H Hamao, T Yamamoto, M Sudou, S Mandai, M & Yamamoto, S. (1999) Micro thermoelectric modules and their application to wristwatches as an energy source. In: 18th International conference on thermoelectrics: 301–7.
83. Strasser, M Aigner, R Lauterbach, C Sturm, T.F. Franosch, M & Wachutka, G (2004) Micromachined CMOS thermoelectric generator as on-chip power supply. Sensors and Actuators A 114: 362–70.
84. Ferrari M, Ferrari V, Guizzetti M, Marioli D & Taroni A (2008) Piezoelectric Multifrequency Energy Converter For Power Harvesting In Autonomous Microsystems Sensors and Actuators A 142(1): 329–335.
85. Kim, I.H Jung, H.J Lee, B.M & Jang, S.J (2011) Broadband energy-harvesting using a two degree-of-freedom vibrating body. Applied Phys. Lett. 98:1–3.
86. Lin, S.C Lee, B.S Wu, W.J & Lee, C.K (2009) Multi-cantilever piezoelectric MEMS generator in energy harvesting. IEEE Int. Ultrason. Symp. Proc., 1: 755–758.
87. G.H. Feng, J.C. Hung (2007) Optimal FOM designed piezoelectric microgenerator with energy harvesting in a wide vibration bandwidth. Proc. 2nd IEEE Int. Conf. on Nano/Micro Engineered and Molecular Systems (16–19) January 2007, Bangkok, Thailand) pp. 511–514.
88. Roundy S, Leland S E, Baker J, Carleton E, Reilly E, Lai E, Otis B, Rabaey J M, Sundararajan V & Wright PK (2005) Improving power output for vibration-based energy scavengers, Pervasive. Comput. 4(1): 28–36.
89. Ferrari M, Ferrari V, Guizzetti M, Andò B, Baglio S & Trigona C (2010) Improved energy harvesting from wideband vibrations by nonlinear piezoelectric converters Sensors and Actuators A: Physical 162(2): 425–31.
90. Cottone F, Gammaitoni L, Vocca H, Ferrari M & Ferrari V (2012) Piezoelectric buckled beamsfor randomvibration energy harvesting. Smart Materials and Structures 21 035021.
91. Liu WQ, Badel A, Formosa F, Wu Y & Agbossou A (2013) Novel piezoelectric bistable oscillator architecture for wideband vibration energy harvesting. Smart Materials and Structures 22(3) 035013.

92. Xue, H Hu, Y & Wang, Q.M (2008) Broadband piezoelectric energy harvesting devices using multiple bimorphs with different operating frequencies. IEEE T. Ultrason. Ferr., 55: 2104–8
93. Shahruz S.M (2006) Design of mechanical band-pass filters for energy scavenging. J. Sound Vib. 292: 987–998.
94. Morgan Electro Ceramics Inc. (2013) material datasheet URI: http://www.morganelectroceramics.com Cited 2013/10/12
95. Mitcheson, P. D Reilly, E. K Toh, T Wright, P. K & Yeatman, E. M. Performance limits of the three MEMS inertial energy generator transduction types. J. Micromech. Microeng., 2007, 17(9): 211–6.
96. Howells CA (2008) Piezoelectric Energy Conversion using Locomotion. American Society of Mechanical Engineers, 2nd International Conference on Energy Sustainability ES2008-54063: 13–17.
97. Rocha JG, Goncalves LM, Rocha PF, Silva MP & Lanceros-Mendez S (2010) Energy harvesting from piezoelectric materials fully integrated in footwear. IEEE Transactions on Industrial Electronics 57(3): 813–19.
98. Pozzi M, Aung MSH, Zhu M, Jones RK & Goulermas JY (2012) The pizzicato knee-joint energy harvester: characterization with biomechanical data and the effect of backpack load. Smart Materials and Structures 21(7)
99. Feenstra J, Granstrom J & Sodano H (2008) Energy harvesting through backpack employing a mechanically amplified piezoelectric stack. Mechanical systems and Signal processing 22(3): 721-34.
100. S.E. Jo, M.K. Kim, M.S. Kim and Y.J. Kim (2012) Flexible thermoelectric generator for human body heat energy harvesting, Electronics letters, 48(16)
101. Dogan, A Fernandez, J.F Uchino, K & Newnham, R.E (1996) The "cymbal" ™ electromechanical actuator, Proc. 10th IEEE Symp. Appl. Ferroelect. 213–6.
102. Lam, K.H Wang, X.X & Chan, H.L.W (2005) Lead-free piezoceramic cymbal actuator. Sensors and Actuators A: Physical 125(2): 393–7.
103. Meyer, R.J Hughes, W.J Montgomery, T,C Markley, D.C & Newnham R.E (2002) Design of fabrication improvements to the cymbal transducer aided by finite element analysis. Journal of Electroceramics 8: 163–74.
104. Ochoa, P Villegas, M Pons, J.L Leidinger, P & Fernández, J.F (2005) Tunability of cymbals as piezocomposite transducers. Journal of Electroceramics 14: 221–9.
105. Tressler, J.F Cao, W Uchino, K & Newnham R.E (1998) Finite element analysis of the cymbal-type flextensional transducer. IEEE Transactions on Ultrasonics, Ferroelectrics and Frequency Control 45(5): 1363–9.
106. Narayanan, M & Schwartz RW (2010) Design, fabrication and finite element modelling of a new wagon wheel flextensional transducer. Journal of Electroceramics 24(3): 205–13.
107. Wang, B & Xia, Q (2008) Numerical analysis on two kinds of cymbal membranes for piezoelectric micro-flow actuator. Journal of Intelligent Material Systems and Structures 19(3): 343–9

108. Kim, H.W Priya, S Uchino, K & R,E Newnham (2005) Piezoelectric energy harvesting under high pre-stressed cyclic vibrations. Journal of Electroceramics 15: 27–34.
109. Kim, H. W Batra, A Priya, S Uchino, K., Markley, D., Newnham, R. E & Hofmann, H (2004) Energy Harvesting Using a Piezoelectric "Cymbal" Transducer in Dynamic Environment. Japanese Journal of Applied Physics 43: 6178–83.
110. Sohn, J.W Choi, S.B & Lee, D.Y (2005) An investigation on piezoelectric energy harvesting for MEMS power sources. Proceedings of the Institution of Mechanical Engineers, Part C: Journal of Mechanical Engineering Science 219(4): 429–436.
111. Mo, C Arnold, D Kinsel, W.C & Clark W.W (2013) Modeling and experimental validation of unimorph piezoelectric cymbal design in energy harvesting. Journal of Intelligent Material Systems and Structures. 24(7): 828–36.
112. Yuan, J Shan, X Xie, T & Chen, W (2010) Modeling and improvement of a cymbal transducer in energy harvesting. Journal of Intelligent Material Systems and Structures 21(8): 765–71.
113. Živanović S, Racić V, El-Bahnasy I & Pavić A (2007) Statistical characterisation of parameters defining human walking as observed on an indoor passerelle. Experimental vibration analysis for civil engineering structures: 219–225.
114. Matsumoto Y, Nishioka T, Shiojiri H & Matsuzaki K (1978) Dynamic design of footbridges. IABSE proceedings P(17): 1–15.
115. Pachi, A & Ji, T (2005) Frequency and velocity of people walking. Struct Eng, 83(3): 36–40.

Original papers

I Leinonen M, Juuti J & Jantunen H (2005) Equivalent circuit based modification of a pre-stressed piezo actuator. Proc. 4th Int. Conf. on Smart Systems, Seinäjoki.

II Sobocinski M, Leinonen M, Juuti J & Jantunen H (2012) A Piezoelectric Active Mirror Suspension System Embedded Into Low-Temperature Cofired Ceramic. IEEE trans. on Ultrasonics, Ferroelectrics and frequency control 59(9): 1990–1995.

III Leinonen M, Palosaari J, Juuti J & Jantunen H (2011) Piezoelectric energy harvester for vibrating environments using multiple beam topology for wideband operation. AP XIX Proceedings 41, Helsinki.

IV Sobocinski M, Leinonen M, Juuti J & Jantunen H (2011) Monomorph piezoelectric wideband energy harvester integrated into LTCC. Journal Of European Ceramic Society 31(5): 789–794.

V Leinonen M, Palosaari J, Juuti J & Jantunen H (2014) Combined electrical and electromechanical simulations of a piezoelectric Cymbal harvester for energy harvesting from walking. Journal of Intelligent Material Systems and Structures, 25(4): 391–400.

514. Sobocinski, Maciej (2014) Embedding of bulk piezoelectric structures in Low Temperature Co-fired Ceramic

515. Kulju, Timo (2014) Utilization of phenomena-based modeling in unit operation design

516. Karinkanta, Pasi (2014) Dry fine grinding of Norway spruce (*Picea abies*) wood in impact-based fine grinding mills

517. Tervo, Valtteri (2015) Joint multiuser power allocation and iterative multi-antenna receiver design

518. Jayasinghe, Laddu Keeth Saliya (2015) Analysis on MIMO relaying scenarios in wireless communication systems

519. Partala, Juha (2015) Algebraic methods for cryptographic key exhange

520. Karvonen, Heikki (2015) Energy efficiency improvements for wireless sensor networks by using cross-layer analysis

521. Putaala, Jussi (2015) Reliability and prognostic monitoring methods of electronics interconnections in advanced SMD applications

522. Pirilä, Minna (2015) Adsorption and photocatalysis in water treatment : active, abundant and inexpensive materials and methods

523. Alves, Hirley (2015) On the performance analysis of full-duplex networks

524. Siirtola, Pekka (2015) Recognizing human activities based on wearable inertial measurements : methods and applications

525. Lu, Pen-Shun (2015) Decoding and lossy forwarding based multiple access relaying

526. Suopajärvi, Terhi (2015) Functionalized nanocelluloses in wastewater treatment applications

527. Pekuri, Aki (2015) The role of business models in construction business management

528. Mantere, Matti (2015) Network security monitoring and anomaly detection in industrial control system networks

529. Piri, Esa (2015) Improving heterogeneous wireless networking with cross-layer information services

530. Leppänen, Kimmo (2015) Sample preparation method and synchronized thermography to characterize uniformity of conductive thin films

Book orders:
Granum: Virtual book store
http://granum.uta.fi/granum/

UNIVERSITY OF OULU P.O. Box 8000 FI-90014 UNIVERSITY OF OULU FINLAND

ACTA UNIVERSITATIS OULUENSIS

UNIVERSITY of OULU
OULUN YLIOPISTO

ISBN 978-952-62-0836-7 (Paperback)
ISBN 978-952-62-0837-4 (PDF)
ISSN 0355-3213 (Print)
ISSN 1796-2226 (Online)